Blast analysis of enclosure masonry walls using homogenization approaches

Gabriele Milani[(1)], Paulo B. Lourenço[(2)]

(1) Corresponding Author. Dipartimento di Ingegneria Strutturale (DIS), Politecnico di Milano, Piazza Leonardo da Vinci 32, 20133 Milano, Italy. E-mail: milani@stru.polimi.it.

(2) ISISE, Department of Civil Engineering, School of Engineering, University of Minho, Azurém, 4800-058 Guimarães, Portugal. E-mail: pbl@civil.uminho.pt.

Abstract

A simple rigid-plastic homogenization model for the analysis of enclosure masonry walls subjected to blast loads is presented. The model is characterized by a few material parameters, is numerically inexpensive and very stable, and allows full parametric studies of entire walls subject to blast pressures.
With the aim of considering the actual brickwork strength along vertical and horizontal axes, masonry out-of-plane anisotropic failure surfaces are obtained by means of a compatible homogenized limit analysis approach. In the model, a 3D system of rigid infinitely strong bricks connected by joints reduced to interfaces is identified with a 2D Kirchhoff-Love plate. For the joints, which obey an associated flow rule, a Mohr-Coulomb failure criterion with a tension cut-off and a linearized elliptic compressive cap is considered. In this way, the macroscopic masonry failure surface is obtained as a function of the macroscopic bending, torque and in-plane forces by means of a linear programming problem in which the internal power dissipated is minimized.
Triangular Kirchhoff-Love elements with linear interpolation of the displacements field and constant moment within each element are used at a structural level. In this framework, a simple quadratic programming problem is obtained to analyze entire walls subjected to blast loads.
The multi-scale strategy presented is adopted to predict the behavior of a rectangular wall supported on three sides (left, bottom and right) representing an envelope wall in a building and subjected to a standardized blast load. The top edge of the wall is assumed unconstrained due to an imperfect connection (often an interlayer material is used to prevent damage in the infill wall). A comparison with a standard elastic-plastic heterogeneous 3D analysis conducted with a commercial FE code is also provided for a preliminary verification of the procedure at a structural level. The good agreement found and the very limited computational effort required for the simulations conducted with the presented model indicate that the proposed simple tool can be used by practitioners for the safety assessment of out-of-plane loaded masonry panels subjected to blast loading. An exhaustive parametric analysis is finally conducted with different wall thicknesses, joint tensile strength and dynamic pressures, corresponding to blast loads (in kg of TNT) ranging from small to large.

Keywords: Masonry, out-of-plane loads, homogenization, dynamic rigid-plasticity, blast pressures.

1 Introduction

Structures and buildings are occasionally called upon to withstand dynamic loading regimes, caused by accidental events, such as for instance impacts (vehicles) or explosions (gas / terrorism). In order to take into account the effect induced on structures by exceptional loads (as for instance explosions), codes of practice of many countries (see the European Code EC1 2006) require the safety assessment of buildings when subjected to *ad-hoc* equivalent static loads. Such loads are usually obtained through empirical coefficients and are aimed to mimic the effect of quasi instantaneous dynamic actions.

An alternative to the static load distributions approach, usually based on simplifications and rules of thumbs, is the utilization of sophisticated finite element non-linear dynamic analyses (Burnett et al. 2007, Wu and Hao 2006 and 2008), usually performed by means of commercial software available in the market. Nevertheless, when dealing with blast loads on masonry structures, a non-linear standard dynamic finite element approach presents a number of drawbacks that limits its applicability to walls of small dimensions, basically for research purposes. Among other factors, the most important aspect is the considerable expertise needed to perform such kind of analysis. Furthermore, computational cost is usually prohibitive even for small walls with a low number of bricks, due to the need of modeling separately mortar joints and units in the framework of a heterogeneous approach. Finally, modeling cracking of joints between masonry units makes the non-linear dynamic analysis difficult and makes the input parameters selection a crucial issue. As a consequence, despite the importance of the problem and the growing interest in the scientific community with respect to the safety assessment of structures subjected to quasi instantaneous dynamic loads, only a few works have been presented in the technical literature, e.g. Wu and Hao (2006 and 2008), Gilbert et al. (1998 and 2002), Mayrhofer (2002).

In this framework, it appears necessary to develop a FE numerical approach for masonry subjected to blast loads that avoids independent modeling of bricks and mortar joints, and is able to reproduce failure mechanisms and the displacements evolution at successive time steps. With this aim, a rigid-plastic FE model for the dynamic analysis of masonry walls is presented, in which out-of-plane anisotropic masonry failure surfaces are obtained by means of a simplified homogenization model.

Masonry skeleton is represented by a 3D discrete system of blocks interacting through interfaces (mortar joints). Blocks are supposed infinitely resistant, whereas for joints a Mohr Coulomb failure criterion for representing frictional phenomena with tension cut-off and compressive limited strength is adopted. In this way, a full description of the model can be given considering a representative volume constituted by a generic brick with its 6 neighbors. In order to obtain a

Kirchhoff-Love equivalent plate, a sub-class of motions for the representative volume is a-priori assumed, so that horizontal flexure, vertical flexure and torsion are reproduced. Then, a numerical procedure of identification between the 3D discrete Lagrangian system and a continuum equivalent model is implemented. Such identification is based on a simple correspondence between motions in the 3D discrete model and the continuum.

In the limit analysis model proposed, which requires a C0 continuity of the displacements field in the elastic range, discontinuous velocity fields can be assumed at the interfaces between adjacent blocks. This allows an accurate description of the actual out-of-plane failure mechanisms, mainly concentrated at the bond between mortar and bricks. Since internal dissipation can take place only at the interface between bricks, a simple constrained minimization problem in few variables is obtained. Macroscopic masonry failure surfaces are numerically evaluated as a function of the macroscopic bending and torsional moments and in-plane actions.

At structural level, triangular Kirchhoff-Love elements with linear interpolation of the displacements field and constant moment within each element are used (Hellan 1967, Herrmann 1967). With the aim of numerically evaluating nodal displacements and internal actions at successive time steps, the simple quadratic programming approach proposed in (Capurso 1972a and 1972b) is adopted.

In order to test the capabilities of the model proposed, a full set of examples of technical interest is analyzed, consisting of an enclosure masonry wall of dimensions 5.60×2.80 m subjected to blast pressure. As preliminary verification of the procedure proposed, results in terms of deformed shapes at successive time steps and time-maximum displacement curves are compared with those provided by a heterogeneous 3D analysis conducted through standard commercial software. Considering both the good agreement of the results obtained with respect to the standard code and the very limited computational effort required for the homogenized rigid-plastic simulations, a full parametric analysis varying wall thickness, mortar joints mechanical properties and loads intensity (i.e. increasing kg of TNT, Bangash and Bangash 2006) is presented at the end of the paper. In particular, for a fixed blast load (TNT mass), joint tensile strength and wall thickness, the maximum displacement reached at the end of the simulations is reported, thus providing simple charts for preliminary assessment or design of enclosure masonry systems.

2 Masonry out-of-plane failure surface

2.1 Basic assumptions

In this section, a procedure to build a Kirchhoff-Love plate model based on a correspondence between equivalent class of motions in a 3D discrete blocks system and a plate continuous model is

presented. The two models are described separately and then an equivalence procedure between the kinematic descriptors in the two systems is performed, in order to study masonry as a 2D thick plate. It is worth noting that the formulation of the model does not impose a field local solution as, for instance, occurs using standard homogenization procedures, but imposes only a kinematic correspondence between motions. This assumption implies that the obtained solution is kinematically admissible.

2.2 Heterogeneous model

Masonry is represented by infinitely resistant blocks connected by mortar joints reduced to interfaces with rigid-plastic behavior (Figure 1). The motion of a generic block A may be described as a function of its center velocity $\mathbf{v}^{C_A} = \left[v_{xx}^{C_A} \;\; v_{yy}^{C_A} \;\; v_{zz}^{C_A} \right]^T$ and its angular velocity $\mathbf{\Phi}^A = \left[\Phi_{xx}^A \;\; \Phi_{yy}^A \;\; \Phi_{zz}^A \right]^T$. Starting from this assumption, the motions of all the blocks in contact to block A may be described. Hence, to describe the kinematic model it suffices to take into consideration the interaction of a generic couple of blocks, (A, B).

Let the point $\boldsymbol{\xi}$ (local coordinates ξ_1, ξ_2) be a generic point on the interface I between A and B, as illustrated in Figure 2. Since $\boldsymbol{\xi} \in I$ belongs respectively to A and B (where I indicates the common interface between the two bricks), the following relations can be written:

$$\begin{aligned} \mathbf{v}^A(\boldsymbol{\xi}) &= \mathbf{v}^{C^A} + \mathbf{M}(\mathbf{\Phi}^A)(\boldsymbol{\xi} - \mathbf{C}^A) \\ \mathbf{v}^B(\boldsymbol{\xi}) &= \mathbf{v}^{C^B} + \mathbf{M}(\mathbf{\Phi}^B)(\boldsymbol{\xi} - \mathbf{C}^B) \end{aligned} \qquad (1)$$

Here, $\mathbf{v}^A(\boldsymbol{\xi})$ ($\mathbf{v}^B(\boldsymbol{\xi})$) is the velocity of point $\boldsymbol{\xi}$, which is considered belonging to block A (B) and $\mathbf{M}(\mathbf{\Phi})$ is the following 3×3 skew matrix:

$$\mathbf{M}(\mathbf{\Phi}) = \begin{bmatrix} 0 & -\Phi_{zz} & \Phi_{yy} \\ \Phi_{zz} & 0 & -\Phi_{xx} \\ -\Phi_{yy} & \Phi_{xx} & 0 \end{bmatrix} \qquad (2)$$

In equation (1), the position $\boldsymbol{\xi}$ of point $\mathbf{P}$ is evaluated with respect to a local frame $(\xi_1 \;\; \xi_2)$ with origin on the centroid on the interface, see Figure 2. It is worth mentioning that the kinematic model here proposed is restricted to small rotation rates. The jump of velocity $[\mathbf{v}(\boldsymbol{\xi})]$ between bricks A and B in a point $\boldsymbol{\xi} \in I$ is expressed by:

$$\lfloor \mathbf{v}(\boldsymbol{\xi}) \rfloor = \mathbf{v}^B(\boldsymbol{\xi}) - \mathbf{v}^A(\boldsymbol{\xi}) = \mathbf{v}^{C^A} - \mathbf{v}^{C^B} + \mathbf{M}(\mathbf{\Phi}^A)(\boldsymbol{\xi} - \mathbf{C}^A) - \mathbf{M}(\mathbf{\Phi}^B)(\boldsymbol{\xi} - \mathbf{C}^B) \qquad (3)$$

and the power dissipated at the interface I can be written as:

$$\pi = \int_I \left[\mathbf{t}^A(\xi) \cdot \mathbf{v}^A(\xi) + \mathbf{t}^B(\xi) \cdot \mathbf{v}^B(\xi) \right] dS = \int_I \mathbf{t}^A(\xi) \cdot \left[\mathbf{v}(\xi) \right] dS \tag{4}$$

where $\mathbf{t}^A(\xi) = \left[\tau_{13}(\xi) \;\; \tau_{23}(\xi) \;\; \sigma_{33}(\xi) \right]^T$ ($\mathbf{t}^B(\xi)$) is the stress vector acting at ξ on brick A (B), see Figure 2, with $\mathbf{t}^A(\xi) = -\mathbf{t}^B(\xi)$

2.3 Continuous model

A standard 2D Cauchy continuum, identified by its middle plane S of normal $\mathbf{e}_3$ (Figure 3), is assumed as an equivalent plate homogenized model. The velocity field of a point **P** (coordinates $\left[x_1^P \;\; x_2^P \;\; x_3^P \right]$) belonging to the equivalent continuum plate is given by fields $\mathbf{w}(\mathbf{x})$ (components w_1, w_2 and w_3) and $\boldsymbol{\Psi}(\mathbf{x})$ (components Ψ_1 and Ψ_2), representing respectively the velocity and rotations rates of the plate in correspondence of the point $\mathbf{x} = \left[x_1^P \;\; x_2^P \;\; 0 \right]$ laying in the middle plane of the plate.

The stored energy density in the equivalent plate model is:

$$\pi = \left[N_{11} \;\; N_{12} \;\; N_{22} \right] \begin{bmatrix} \dot{E}_{11} \\ \dot{E}_{12} + \dot{E}_{21} \\ \dot{E}_{22} \end{bmatrix} + \left[T_{13} \;\; T_{23} \right] \begin{bmatrix} \dot{\gamma}_{13} \\ \dot{\gamma}_{23} \end{bmatrix} + \left[M_{11} \;\; M_{12} \;\; M_{22} \right] \begin{bmatrix} \dot{\chi}_{11} \\ \dot{\chi}_{12} + \dot{\chi}_{21} \\ \dot{\chi}_{22} \end{bmatrix} \tag{5}$$

where:

- $\dot{\mathbf{E}} = \begin{bmatrix} \dot{E}_{11} \\ \dot{E}_{12} + \dot{E}_{21} \\ \dot{E}_{22} \end{bmatrix} = \frac{1}{t} \int_{-t/2}^{t/2} \begin{bmatrix} \partial w_1 / \partial x_1 - x_3 \partial \Psi_1 / \partial x_1 \\ \partial w_2 / \partial x_1 + \partial w_1 / \partial x_2 - x_3 \left(\partial \Psi_1 / \partial x_2 + \partial \Psi_2 / \partial x_1 \right) \\ \partial w_2 / \partial x_2 - x_3 \partial \Psi_2 / \partial x_2 \end{bmatrix} dx_3$ (in-plane strain rate vector, assuming as t masonry thickness);

- $\dot{\boldsymbol{\gamma}} = \begin{bmatrix} \dot{\gamma}_{13} \\ \dot{\gamma}_{23} \end{bmatrix} = \frac{1}{t} \int_{-t/2}^{t/2} \begin{bmatrix} \partial w_3 / \partial x_1 + \partial w_1 / \partial x_3 \\ \partial w_3 / \partial x_2 + \partial w_2 / \partial x_3 \end{bmatrix} dx_3$ (shear strain rate);

- $\dot{\boldsymbol{\chi}} = \begin{bmatrix} \dot{\chi}_{11} \\ \dot{\chi}_{12} + \dot{\chi}_{21} \\ \dot{\chi}_{22} \end{bmatrix} = \frac{1}{t} \int_{-t/2}^{t/2} \begin{bmatrix} \partial \Psi_1 / \partial x_1 \\ \partial \Psi_2 / \partial x_1 + \partial \Psi_1 / \partial x_2 \\ \partial \Psi_2 / \partial x_2 \end{bmatrix} dx_3$ (strain rate vector);

- $\mathbf{M} = \left[M_{11} \;\; M_{12} \;\; M_{22} \right]^T$, with M_{11} and M_{22} indicating bending and M_{12} torsion;

- $\mathbf{T} = \left[T_{13} \;\; T_{23} \right]^T$;

- $\mathbf{N} = \left[N_{11} \;\; N_{12} \;\; N_{22} \right]^T$.

It is worth noting that, despite the fact that a full Reissner-Mindlin plate theory can be developed with the model proposed, here a 2D Kirchhoff-Love approach is adopted. This is possible adding

the further kinematic constraint $\dot{\boldsymbol{\gamma}} = \mathbf{0}$ at a cell level. The reason of limiting the study to thin plates is justified by the relatively high slenderness of the walls analyzed. It has been demonstrated, in fact (see Milani et al. 2006c), that a Kirchhoff-Love approach is able to give accurate results in the inelastic range for such cases, especially when running bond is adopted for the masonry.

2.4 Simplified homogenization

In order to substitute the heterogeneous material with the homogeneous equivalent 2D model, see Figure 4, a simple compatible identification model is proposed, assuming that the power dissipated by blocks assemblage (equation (4)) is equal to the power dissipated by the equivalent model, equation (5). For this purpose, fields $\mathbf{w}(\mathbf{x})$ and $\boldsymbol{\Psi}(\mathbf{x})$ are a priori chosen as a combination of elementary deformations in the unit cell, corresponding to actual failure mechanisms occurring in presence of running bond brickwork with weak joints reduced to interfaces. From a practical point of view, fields $\mathbf{w}(\mathbf{x})$ and $\boldsymbol{\Psi}(\mathbf{x})$, corresponding to each sub-class of regular motions, are obtained assuming alternatively one component of vector $\dot{\mathbf{E}}$, $\dot{\boldsymbol{\gamma}}$ or $\dot{\boldsymbol{\chi}}$ unitary and setting all the other components equal to zero, subsequently choosing the most simple polynomial expressions for $\mathbf{w}(\mathbf{x})$ and $\boldsymbol{\Psi}(\mathbf{x})$ that comply with equation (5). Once fields $\mathbf{w}(\mathbf{x})$ and $\boldsymbol{\Psi}(\mathbf{x})$ are known, rotations rates and velocities of each brick belonging to the REV in the heterogeneous model are determined assuming as point $\mathbf{x}$ the centroid of the brick under consideration.

For instance, when only $\dot{\boldsymbol{\chi}}_{11} \neq 0$ is applied on the REV, a choice for $\mathbf{w}(\mathbf{x})$ and $\boldsymbol{\Psi}(\mathbf{x})$ fields is:

$$\begin{aligned} \Psi_1 &= \dot{\chi}_{11} x_1 \\ w_1 &= \dot{\chi}_{11} x_1 x_3 \\ w_2 &= 0 \\ w_3 &= -\dot{\chi}_{11} x_1^2 / 2 \end{aligned} \qquad (6)$$

Equation (6) allows to directly determine velocities and rotations of each block, provided that the coordinates of the respective centroid are introduced in (6).

Since a Kirchhoff-Love plate approach is adopted to study blasts at a structural level, it is possible to limit the study at the micro-scale to in-plane actions, out-of-plane bending and torsion (i.e. $\dot{\mathbf{E}}$ and $\dot{\mathbf{M}}$ respectively). For instance, Figure 5-a shows the effect on the brickwork of a homogeneous deformation $\chi_{11} \neq 0$ with all the other strain measures set to zero. It must be noted that both head and bed joints are involved in the dissipation induced by this deformation. Figure 5-b shows the effect on the brickwork of a homogeneous deformation in which $\chi_{22} \neq 0$ and all the other strain measures are set to zero. In this case, it is interesting to note that only the bed joints present a relative jump of velocities between adjacent bricks. Similarly, in Figure 5-c and -d the cases $\chi_{12} \neq 0$ and $\chi_{21} \neq 0$ are

examined. In the first case, no bending moment is present in the head joints, whereas there is torsion of the bed joints. On the contrary, in the second case, torsion is present in the head joints and bending moment acts in the bed joints.

2.5 Unreinforced masonry failure surfaces

In this section, after the original formulation by Suquet (1983), a general numerical procedure for obtaining macroscopic in- and out-of-plane unreinforced masonry failure surfaces is presented. Strength domains for periodic arrangements of heterogeneous materials can be obtained by means of a combined homogenization and limit analysis approach. Both static and kinematic theorems of limit analysis can be used for this purpose. In this framework, it is worth noting that several different models have been presented in the literature for the evaluation of both in-plane (e.g. Milani et al. 2006a and 2006b) and out-of-plane masonry failure surfaces (Milani et al. 2006c and Cecchi and Milani 2008).

One of the basic assumptions of this approach is the utilization of associated flow rules for the constituent materials. Nevertheless, it is worth mentioning that sliding occurs in mortar joints with almost zero dilatancy, with typical non-associativity. The violation of one of the hypothesis of classic limit analysis (Orduna and Lourenço 2005, Ferris and Tin-Loi 2001, etc.), implies that the uniqueness of the ultimate load may be lost and a multiplicity of solutions can exist, see Begg and Fishwick (1995). On the contrary, the assumption of associated flow rules ensures the uniqueness of the ultimate load factor and leads to simple optimization problems which can be handled easily with linear programming (LP) packages. In any case, it has been demonstrated that associated limit analysis gives reliable results when failure mechanisms are mainly due to tensile cracking of the joints (see for instance Sinha 1978, Lourenço et al. 1998). As out-of-plane masonry failure occurs by triggering the joints tensile regime, associated limit analysis seems adequate. A failure criterion $\phi = \phi(\boldsymbol{\sigma})$ for the joints must be incorporated. The basic failure modes for masonry walls with weak mortar are a mixing of sliding along the joints (a), cracking of the joints (b) and compressive masonry crushing (c). These modes can be well reproduced adopting a Mohr-Coulomb failure criterion combined with a tension cut-off and a cap in compression, see Figure 6, as suggested by Lourenço and Rots (1997).

Aiming at treating the problem in the framework of linear programming, within each interface I of area A^I, a piecewise linear approximation of the failure surface $\phi = \phi(\boldsymbol{\sigma})$ is adopted, constituted by n_{lin} planes of equation $\mathbf{A}_i^{I\,T}\boldsymbol{\sigma} = c_i^I \quad 1 \le i \le n_{lin}$, where $\boldsymbol{\sigma} = [\sigma_{33} \;\; \tau_{13} \;\; \tau_{23}]$, σ_{33} is the normal stress on the interface and τ_{13} and τ_{23} are tangential stresses along two assigned perpendicular directions

($A_i^{1I}\sigma_{33} + A_i^{2I}\tau_{13} + A_i^{3I}\tau_{23} = c_i^I$ is the i-th linearization plane of the interface I, with $\mathbf{A}_i^{IT} = \left[A_i^{1I} \;\; A_i^{2I} \;\; A_i^{3I}\right]$), Figure 2 and Figure 6.

The jump of velocity on interfaces varies linearly in the discrete model, equation (3). Thus, for each interface, only $3 \cdot n_{lin}$ independent plastic multiplier rates have to be introduced as optimization variables. Furthermore, for each interface I between contiguous bricks, the following equality constraints between plastic multiplier rates $\dot{\lambda}_i^I(\xi_1, \xi_2)$ and jump of velocity $\left[\mathbf{v}(\xi_1, \xi_2)\right]$ on the interface must be imposed:

$$\left[\mathbf{v}(\xi_1, \xi_2)\right] = \sum_{i=1}^{n_{lin}} \dot{\lambda}_i^I(\xi_1, \xi_2) \frac{\partial \phi}{\partial \boldsymbol{\sigma}} \qquad (7)$$

where:

- $\boldsymbol{\xi} = (\xi_1, \xi_2)$ is a local frame of reference laying on the interface plane and with axis ξ_3 orthogonal to the interface plane, Figure 2 and Figure 6;

- $\left[\mathbf{v}(\xi_1, \xi_2)\right] = \left[\Delta v_{33} \;\; \Delta v_{13} \;\; \Delta v_{23}\right]^T$ is the jump of velocity field (linear in (ξ_1, ξ_2)) on the I-th interface and Δv_{ij} corresponds to the jump along the direction j.

- $\dot{\lambda}_i^I(\xi_1, \xi_2)$ is the i-th plastic multiplier rate field (linear in (ξ_1, ξ_2)) of the interface I, associated to the i-th linearization plane of the failure surface.

It is worth noting that, in order to satisfy equation (7) for each point of the interface I, nine equality constraints for each interface have to be imposed, which corresponds to evaluating (7) in three different positions $P_k = \left(\xi_1^{P_k}, \xi_2^{P_k}\right)$ on the interface I as follows:

$$\left[\mathbf{v}\left(\xi_1^{P_k}, \xi_2^{P_k}\right)\right] = \sum_{i=1}^{n_{lin}} \dot{\lambda}_i^I\left(\xi_1^{P_k}, \xi_2^{P_k}\right) \frac{\partial \phi}{\partial \boldsymbol{\sigma}} \quad k = 1,2,3 \qquad (8)$$

Here, $\dot{\lambda}_i^I\left(\xi_1^{P_k}, \xi_2^{P_k}\right)$ is the is i-th plastic multiplier rate of the interface I corresponding to $P_k = \left(\xi_1^{P_k}, \xi_2^{P_k}\right)$.

From the previous equations, the internal power dissipated on the I-th interface can be written as:

$$\pi_{\text{int}}^I = \int_{A^I} [\mathbf{v}]^T \boldsymbol{\sigma} dA^I = \int_{A^I} \sum_{i=1}^{n_{lin}} \dot{\lambda}_i^I(\xi_1, \xi_2) \left[\frac{\partial \phi}{\partial \boldsymbol{\sigma}}\right]^T \boldsymbol{\sigma} dA^I = \frac{1}{4} \sum_{i=1}^{n_{lin}} c_i^I \sum_{k=1}^{4} \dot{\lambda}_i^I\left(\xi_1^{P_k}, \xi_2^{P_k}\right) A^I \qquad (9)$$

It is worth noting that in equation (9) only three of the four plastic multipliers are linearly independent, whereas $k = 4$ depends linearly on $k = 1,2,3$ (the plastic multiplier field is linear on the interface).

The external power dissipated can be written as $\pi_{ext} = \left(\boldsymbol{\Sigma}_0^T + \lambda \boldsymbol{\Sigma}_1^T\right)\mathbf{D}$, where $\boldsymbol{\Sigma}_0$ is the vector of permanent loads, λ is the load multiplier, $\boldsymbol{\Sigma}_1^T$ is the unitary vector of loads dependent on the load

multiplier (i.e. the optimization direction in the space of macroscopic stresses) and $\mathbf{D}$ is the vector of macroscopic kinematic descriptors. $\mathbf{D}$ collects in-plane deformation rates ($\dot{E}_{11}$ $0.5\left(\dot{E}_{12}+\dot{E}_{21}\right)\dot{E}_{22}$) and Kirchhoff-Love out-of-plane curvature rates ($\dot{\chi}_{11}$ $\left(\dot{\chi}_{12}+\dot{\chi}_{21}\right)/2$ $\dot{\chi}_{22}$). As the amplitude of the failure mechanism is arbitrary, a further normalization condition $\mathbf{\Sigma}_1^T\mathbf{D}=1$ is usually introduced. Hence, the external power becomes linear in $\mathbf{D}$ and λ and can be written as follows $\pi_{ext}=\mathbf{\Sigma}_0^T\mathbf{D}+\lambda$.

From the above considerations, optimization variables necessary to determine masonry homogenized strength domain are respectively the vector of macroscopic kinematic descriptors $\mathbf{D}$ and the vector of assembled plastic multiplier rates $\dot{\boldsymbol{\lambda}}^I$ at each mortar interface.

From equations (6) and (3), a further set of linear equality constraints has to be imposed at each interface I, involving vector $\mathbf{D}$ and jump of displacements field $\left[\mathbf{v}\left(\xi_1,\xi_2\right)\right]$:

$$\left[\mathbf{v}\left(\xi_1,\xi_2\right)\right]=\mathbf{G}^I\left(\xi_1,\xi_2\right)\mathbf{D} \qquad (10)$$

where $\mathbf{G}^I\left(\xi_1,\xi_2\right)$ is a 3x5 matrix that depends only on the geometry of the interface under consideration (see Figure 6). It is interesting to notice that, from equations (8) and (10), the jump of velocities $\left[\mathbf{v}\left(\xi_1,\xi_2\right)\right]$ does not enter as optimization variable in the optimization problem at a cell level, being $\mathbf{G}^I\left(P_k\right)\mathbf{D}=\left[\mathbf{v}\left(P_k\right)\right]=\sum_{i=1}^{n_{lin}}\dot{\lambda}_i^I\left(\xi_1^{P_k},\xi_2^{P_k}\right)\frac{\partial\phi}{\partial\boldsymbol{\sigma}}$ $P_k\in I$. In particular, from equations (8), (9), (10) and from the kinematic formulation of limit analysis, the following constrained minimization problem has to be solved to obtain masonry failure surfaces:

$$\begin{cases} \lambda=\min\limits_{\hat{\mathbf{x}}=[\mathbf{D},\lambda_i^I(P_k)]}\sum\limits_{I=1}^{n^I}\pi_{\text{int}}^I-\mathbf{\Sigma}_0^T\mathbf{D} \\ \mathbf{\Sigma}_1{}^T\mathbf{D}=1 \\ \mathbf{G}^I\left(P_k\right)\mathbf{D}=\left[\mathbf{v}\left(P_k\right)\right]=\sum\limits_{i=1}^{n_{lin}}\dot{\lambda}_i^I\left(\xi_1^{P_k},\xi_2^{P_k}\right)\frac{\partial\phi}{\partial\boldsymbol{\sigma}} \quad P_k\in I \end{cases} \qquad (11)$$

Here, n^I is the total number of interfaces considered and $\hat{\mathbf{x}}$ is the vector of total optimization unknowns. The linear programming problem (11) involves a relatively small number of optimization variables and therefore can be solved by means of simplex or interior point methods (vector $\hat{\mathbf{x}}$ of global unknowns collects only $3\cdot n_{lin}\cdot n^I$ plastic multiplier rates and 5 macroscopic kinematic variables $\mathbf{D}$). When it is required to investigate only masonry homogenized flexural behavior under the hypothesis of the thin plate theory, $\mathbf{D}$ is a vector of length six collecting in-plane macroscopic deformation rates ($\dot{E}_{11}$, $0.5(\dot{E}_{12}+\dot{E}_{21})$ and $\dot{E}_{22}$) and curvature rates ($\dot{\chi}_{11}$, $0.5(\dot{\chi}_{12}+\dot{\chi}_{21})$ and $\dot{\chi}_{22}$), whereas masonry macroscopic strength domain is a surface in the six

dimensional space of membrane actions (N_{11}, N_{12} and N_{22}), bending moments (M_{11} and M_{22}) and torsion (M_{12}), i.e. $\hat{\Phi} = \hat{\Phi}(N_{11}, N_{12}, N_{22}, M_{11}, M_{12}, M_{22})$. Obviously, the optimal value λ obtained from (11) represents only a point on $\hat{\Phi}$, i.e. the intersection between surface $\hat{\Phi}$ and the direction unit vector $\boldsymbol{\Sigma}_1$ in the six dimensional space $\boldsymbol{\Sigma} = (N_{11}, N_{12}, N_{22}, M_{11}, M_{12}, M_{22})$, see also Figure 7. Consequently, in order to obtain a reliable linear approximation of $\hat{\Phi}$ by means of Delaunay tessellations, the linear programming problem (11) has to be solved several times, each problem corresponding to a different choice for $\boldsymbol{\Sigma}_1$ direction.

In-plane influence on bending behavior has to be taken into account and, for the sake of simplicity, it is assumed that only vertical membrane load N_{22} (typically due to masonry self weight and dead and live vertical loads acting at the top of the wall) is not negligible. Therefore, despite the fact that in the following section the full case $\hat{\Phi} = \hat{\Phi}(N_{11}, N_{22}, N_{12}, M_{11}, M_{12}, M_{22})$ will be discussed, at structural level only $\hat{\Phi} = \hat{\Phi}(M_{11}, M_{12}, M_{22})$ masonry strength domain projections at fixed vertical membrane load N_{22} will be considered.

2.6 A meaningful application at a cell level

A masonry wall constituted by bricks of dimensions 300×200×150 mm (length × height × thickness) and mortar joints reduced to interfaces is considered. The same geometrical properties adopted here are assumed at a structural level for the dynamic analyses. Mechanical properties at failure adopted for the constituent materials are summarized in Table I. For mortar joints, a linearized Lourenço and Rots (1997) failure criterion is adopted, whereas bricks are assumed infinitely resistant. An ultimate tensile strength of joints f_t equal to 0.2 MPa is assumed for the simulations (case II of Table I).

In Figure 8, $N_h - N_v$ masonry in-plane strength domains obtained with the model proposed are reported for three different orientations of the bed joint (N_v in Figure 8 represents vertical homogenized membrane action). The results show that the model is capable of reproducing the typical anisotropic behavior of masonry along the material axes under in-plane loads. In particular, the masonry macroscopic failure surface is anisotropic in tension and compression (compare Figure 8-a and –b). Since a reliable evaluation of masonry ultimate strength is crucial at structural level (especially when inclined yield lines with respect to bed joint orientation are considered), the model proposed seems suited for the analysis of brickwork panels in flexure.

In Figure 9-a, several sections $M_{11} - M_{22}$ of the masonry failure surface $\hat{\Phi}$ are represented varying N_{22}. In a similar way, in Figure 9-b, the same simulations are repeated representing sections

$M_{11} - M_{12}$. As it is possible to note, vertical membrane load influences not only the horizontal bending moment but also the vertical one, as a consequence of the fact that also bed joints contribute to masonry vertical ultimate moment (frictional behavior). On the other hand, high values of membrane compressive loads reduce masonry out-of-plane strength (due to the limited compressive strength assumed for joints).

Finally, it is stressed that the choice of a failure criterion for joints with frictional behavior combined with a limited compressive and tensile strength is suitable for providing results in agreement with experimental evidences. For the sake of completeness, in Figure 10 a typical deformed shape at collapse for the elementary cell obtained with the kinematic model proposed in case of pure torsion is shown.

3 The FE thin plate triangular formulation

In order to solve blast problems for masonry structures out-of-plane loaded, a FE thin plate triangular formulation based on the plate bending element proposed independently by Hellan (1967) and Herrmann (1967) is used. This triangular element has been preferred to more accurate elements (e.g. Krabbenhoft and Damkilde 2002, Krenk et al. 1994) due to the inherent simplicity and the low number of unknowns involved in the optimization. A constant moment field is assumed inside each element E, so that three moment unknowns per element are introduced; such unknowns are the horizontal, vertical and torsion moments ($M_{xx}^{E}, M_{yy}^{E}, M_{xy}^{E}$) or alternatively three bending moments M_{nn}^{Ei}, M_{nn}^{Ej}, M_{nn}^{Ek} along the edges of the triangle (Figure 11-a). For what concerns the displacement field, the element turns out to be analogous to the Munro and Da Fonseca (1978) triangle. In particular, the displacement field is assumed linear inside each element and nodal displacements are taken as optimization variables. Denoting by $\mathbf{w}_E = \begin{bmatrix} w_i^E & w_j^E & w_k^E \end{bmatrix}^T$ the element E nodal displacements and by $\boldsymbol{\theta}_E = \begin{bmatrix} \vartheta_i^E & \vartheta_j^E & \vartheta_k^E \end{bmatrix}^T$ the side normal rotations, $\boldsymbol{\theta}_E$ and $\mathbf{w}_E$ are linked by the compatibility equation (Figure 12-a and –b):

$$\boldsymbol{\theta}_E = \mathbf{B}_E \mathbf{w}_E \qquad (12)$$

where:

- $\mathbf{B}_E = \frac{1}{2A_E}\begin{bmatrix} \frac{b_i b_i + c_i c_i}{l_i} & \frac{b_i b_j + c_i c_j}{l_i} & \frac{b_i b_k + c_i c_k}{l_i} \\ \frac{b_j b_i + c_j c_i}{l_j} & \frac{b_j b_j + c_j c_j}{l_j} & \frac{b_j b_k + c_j c_k}{l_j} \\ \frac{b_k b_i + c_k c_i}{l_k} & \frac{b_k b_j + c_k c_j}{l_k} & \frac{b_k b_k + c_k c_k}{l_k} \end{bmatrix}$, with $b_i = y_j - y_k$, $c_i = x_k - x_j$ and A_E is the element area.

Plastic dissipation occurs only along each interface I between two adjacent triangles R and K or on a boundary side B of an element Q (see Figure 12-c). Continuity of M_{nn}^E bending moments is imposed for each internal interface between two adjacent elements R and K (i.e. $M_{nn}^{Ri} = M_{nn}^{Kj}$, see Figure 11-b), whereas no constraints are imposed for the torsion moment and the shear force.

Due to the constant assumption for the moment fields, internal equilibrium for each element is ensured only in an integral form. Application element by element of the principle of virtual work, provides three equilibrium equations for each triangle:

$$\mathbf{R}_E + \mathbf{B}_E^T \mathbf{M}_E = \mathbf{P}_E + \mathbf{m}_E \ddot{\mathbf{w}}_E \qquad (13)$$

where

- $\mathbf{R}_E = \begin{bmatrix} R_i & R_j & R_k \end{bmatrix}^T$ are nodal (unknown) reactions, see Figure 11-c;

- $\mathbf{P}_E = \frac{1}{2A_E}\mathbf{T}_E^T \int_E \begin{bmatrix} 1 & x & y \end{bmatrix}^T p(x,y) dA$ ($\mathbf{T}_E^T = \begin{bmatrix} a_i & a_j & a_k \\ b_i & b_j & b_k \\ c_i & c_j & c_k \end{bmatrix}$, $a_i = x_j y_k - x_k y_j$). Note that vector $\mathbf{P}_E$ can be regarded as a lumped load equivalent to the resultant action associated to $p(x,y)$.

- the term $\mathbf{m}_E \ddot{\mathbf{w}}_E$ represents the contribution of inertia forces to the overall equilibrium. Here, matrix $\mathbf{m}_E$ is the matrix of equivalent lumped masses and is obtained analogously to vector $\mathbf{P}_E$ assuming a constant density ρ inside each triangular element.

Further equality constraints have to be imposed in order to ensure nodal equilibrium, i.e. for each (not-constrained) node i the following equation has to be satisfied:

$$\sum_{r=1}^{p} R_i^E = 0 \qquad (14)$$

where R_i^E is referred to element E and p is the number of elements with one vertex in i.

Since moment fields are kept constant for each element E, only one set of admissibility conditions in the linearized form $\mathbf{A}_E^{in}\mathbf{M}_E \le \mathbf{b}_{in}^E$ is required, where $\mathbf{A}_E^{in}$ is a $mx3$ coefficients matrix of the linearization planes of the strength domain, m is the number of the planes in the linearization, $\mathbf{b}_{in}^E$

collects the right hand sides of these planes and $\mathbf{M}_E = \left[M_{xx}^E \quad M_{yy}^E \quad M_{xy}^E \right]^T$ is the vector of element moment unknowns.

4 Dynamic analysis of rigid-plastic plates: a quadratic programming approach

In the field of steel structures, basic theorems concerning rigid-plastic dynamics, as well as models devoted to the evaluation of the effect of impacts (including one degree of freedom mode solution) are well known, go back to 1960's and are due to Martin (1964), Martin and Symonds (1965), Tamuzh (1962), etc.. The main hypotheses of such models are the following (see Capurso 1972a, Cannarozzi and Laudiero 1976, and a more recent paper by Kim and Huh 2006):

1. rigid-perfectly plastic behavior of the material;
2. strain rate insensitivity of the yield stress;
3. negligible changes of the geometry during deformation.

These requirements are somewhat contradictory, since large energy inputs will tend to cause large displacements and high velocities sensibly affect the value of yield stress. In order to circumvent these limitations, extensions to rate dependent materials and large deformations problems were attempted in the first applications (Capurso 1972b). Despite the obvious approximations and limitations connected to the previous hypotheses, it has been shown that rigid-plastic approaches perform well for ductile structural elements subjected to impacts and that experimental data available can be fitted with sufficient accuracy (see for instance Bodner and Symonds 1962). Thus, rigid-perfect plasticity has been used by many authors in design practice to obtain a fast estimate (Martin and Symonds 1965, Komarov and Nemirovskii 1985) of deformations induced by dynamic loads. For masonry structures subjected to static loads, following the pioneering work by Heyman (1969), limit analysis has been extensively utilized (e.g. Orduna and Lourenço 2005).

In analogy to what is proposed in the static case, a rigid-plastic assumption for bricks and mortar joints is attempted, with the aim of analyzing full walls subjected to impacts. Since masonry out-of-plane behavior is mostly related to joints tensile strength (Lourenço 1999), it is expected that the model provides good approximations of experimental results modeling joints with poor mechanical properties. When dealing with rigid-plastic plates discretized by means of triangular elements with linear interpolation of the out-of-plane displacement field, the analysis under impulsive loads can be carried out in the framework of a quadratic programming approach. In particular, within the class of all internal actions and accelerations that are dynamically and plastically admissible (i.e. obeying dynamic equilibrium and belonging to the class of internal actions connected with initial velocities,

so representing a static formulation, see Martin 1964), the actual set minimizes, following the original definition given in Capurso (1972a), the second order kinetic energy of the structure, i.e.:

$$\begin{aligned} &\min\left\{\Omega\left(\ddot{\mathbf{w}}\right)\right\} = \min\left\{\frac{1}{2}\ddot{\mathbf{w}}^T\mathbf{m}\ddot{\mathbf{w}}\right\} \\ &\text{subject to}\begin{cases} \mathbf{R}_E + \mathbf{B}_E^T\mathbf{M}_E = \mathbf{P}_E + \mathbf{m}_E\ddot{\mathbf{w}}\ \forall E & (a) \\ \tilde{\mathbf{A}}^{eq}\tilde{\mathbf{M}} = \tilde{\mathbf{b}}^{eq} & (b) \\ \tilde{\mathbf{A}}^{in}\tilde{\mathbf{M}} \le \tilde{\mathbf{b}}^{in} & (c) \end{cases} \end{aligned} \qquad (15)$$

where:

- $\mathbf{R}_E$, $\mathbf{B}_E$, $\mathbf{P}_E$, $\mathbf{m}_E$, $\ddot{\mathbf{w}}$ have been already introduced in the previous section. Following this notation, $\dot{\mathbf{w}}$ and $\mathbf{w}$ will indicate in the following respectively velocities and displacements nodal vectors.
- $\tilde{\mathbf{M}}$ is the assembled vector of elements internal actions (bending moments);
- $\mathbf{P}_E$ collects the external forces vector, generally dependent on the time step under consideration;
- $\mathbf{m}_E$ is the square matrix of masses, which typically are lumped at each nodal point;
- $\mathbf{B}_E$ is a coefficients' matrix that depends only on size and shape of finite elements utilized.

More in detail, assuming a piecewise linear yield surface for an element E, the set of admissible internal actions states can be expressed by the set of linear inequalities:

$$\left[-\mathbf{A}\mathbf{M}_E + \mathbf{b}\right]\begin{bmatrix} = \\ \ge \end{bmatrix}\left[\mathbf{0}\right] \qquad (16)$$

where we denote with $\mathbf{A} = \left[\mathbf{A}^{eq};\ \mathbf{A}^{in}\right]$ the matrix assembling the components of the outward unit normals to the linearized masonry failure surface hyperplanes and $\mathbf{b} = \left[\mathbf{b}^{eq};\ \mathbf{b}^{in}\right]^T$ represents the vector of the distance of each hyperplane from the origin.

In equation (15), the superscript $\tilde{}$ indicates assembled matrices and vectors corresponding respectively to local elements matrices and vectors. The set of equations (a) in the optimization problem (15) represents dynamic equilibrium condition. The principle of virtual works yields to the corresponding compatibility condition:

$$\tilde{\mathbf{B}}\dot{\mathbf{w}} - \tilde{\dot{\boldsymbol{\varepsilon}}}_{pl} = \mathbf{0} \qquad (17)$$

where $\tilde{\dot{\boldsymbol{\varepsilon}}}_{pl}$ is the assembled plastic strain rate vector.

In equation (15), a partition of matrix $\mathbf{A}$ and vector $\mathbf{b}$ into equalities and inequality constraints is imposed (see equation (16)). In particular, equality constraints represent points at which yielding has been already occurred at the previous time step iteration, whereas inequalities stand for the points at which yielding on a linearization plane can occur.

A so called “kinematic” formulation is also available (Capurso 1972a). In particular, within the class of all accelerations and plastic multiplier rates which are kinematically admissible and obeying an associated flow rule (i.e. which comply with compatibility and with outward normal rule for the set of planes not activated by the initial velocities), the actual set minimizes the sum of the second order kinetic energy and the residual dissipation rate of the structure, i.e.:

$$\min\left\{\Xi\left(\ddot{\mathbf{w}},\ddot{\boldsymbol{\lambda}}\right)\right\}=\min\left\{\frac{1}{2}\ddot{\mathbf{w}}^{T}\mathbf{m}\ddot{\mathbf{w}}-\mathbf{F}(t)^{T}\ddot{\mathbf{w}}+\tilde{\mathbf{b}}^{IT}\ddot{\boldsymbol{\lambda}}\right\}$$
$$\text{subject to}\begin{cases}\tilde{\mathbf{B}}_{E}\ddot{\mathbf{w}}=\tilde{\mathbf{A}}^{I}\ddot{\boldsymbol{\lambda}} & (a)\\ \ddot{\boldsymbol{\lambda}}=\left[\ddot{\boldsymbol{\lambda}}_{y}^{T}\ \ \ddot{\boldsymbol{\lambda}}_{r}^{T}\right]^{T} & (b)\\ \ddot{\boldsymbol{\lambda}}_{r}\geq\mathbf{0} & (c)\end{cases} \qquad (18)$$

where:

- $\ddot{\boldsymbol{\lambda}}$ is the vector of second derivatives of plastic multipliers (in the present case plastic multipliers are referred to each interface). $\ddot{\boldsymbol{\lambda}}=\left[\ddot{\boldsymbol{\lambda}}_{y}^{T}\ \ddot{\boldsymbol{\lambda}}_{r}^{T}\right]^{T}$ is the partitioned $\ddot{\boldsymbol{\lambda}}$ vector, where index y indicates that the corresponding $\dot{\lambda}_{y}\neq 0$, whereas index r indicates that at the previous iteration $\dot{\lambda}_{r}=0$;
- $\mathbf{m}$ is the matrix of masses lumped at nodes;
- $\mathbf{F}(t)$ is the vector of lumped external dynamic actions;
- $\tilde{\mathbf{B}}_{E}$ is the assembled transposed matrix utilized in the static approach (see equation (15)-a). It is interesting to notice that equation (18)-(a) is the assembled compatibility equation already introduced in (12);
- The superscript I indicates quantities (i.e. vectors and matrices) referred to interfaces. It is worth noting that the procedure outlined by Krabbenhoft et al. (2005) was adopted to obtain homogenized masonry strength domains (and hence vectors and matrices in the rotated frame of reference) for an interface with generic orientation ϑ^{I} with respect to horizontal axis.

More in detail, if the vector $\boldsymbol{\lambda}^{E}=\left[\lambda_{1}^{E}\ \lambda_{2}^{E}\ \ldots\ \lambda_{n}^{E}\right]^{T}$ represents plastic multipliers of an element E (or an interface I), the associated flow rule is expressed for each element as:

$$\dot{\boldsymbol{\varepsilon}}_{pl}^{E}=\mathbf{A}^{T}\dot{\boldsymbol{\lambda}}^{E} \qquad (19)$$

where $\dot{\boldsymbol{\varepsilon}}_{pl}^{E}$ is the plastic strain rate vector of element E. In the framework of rigid-perfect plasticity, equation (19) is subjected to the following equality and inequality constraints:

$$\begin{cases}\dot{\boldsymbol{\lambda}}^{E}\geq\mathbf{0}\\ \left(\dot{\boldsymbol{\lambda}}^{E}\right)^{T}\left(-\mathbf{A}\mathbf{M}_{E}+\mathbf{b}\right)=0\end{cases} \qquad (20)$$

$\mathbf{w}$ with its derivatives with respect to time is a function of time, $\dot{\boldsymbol{\varepsilon}}_{pl}^{E}$ and $\dot{\boldsymbol{\lambda}}^{E}$ are also time dependent functions. Thus, equation (19) differentiated with respect to time yields:

$$\ddot{\boldsymbol{\varepsilon}}_{pl}^{E} = \mathbf{A}^{T}\ddot{\boldsymbol{\lambda}}^{E} \qquad (21)$$

Element E (or an interface I), governed by plastic flow law (19), (20) and (21), at a given instant t_0 is in one of the following four cases:

1. if the internal actions vector $\mathbf{M}_E$ is inside the failure surface, then $\dot{\boldsymbol{\varepsilon}}_{pl}^{E} = \mathbf{0}$, implying that:

   $$\dot{\boldsymbol{\lambda}}^{E} = \ddot{\boldsymbol{\lambda}}^{E} = \mathbf{0} \qquad (22)$$

   with an undetermined state for the internal actions state.
2. if the internal actions vector is a regular point of the linearized failure surface (say belonging to the j th hyperplane), but $\dot{\boldsymbol{\lambda}}^{E}(t_0) = \mathbf{0}$, we have:

   $$\begin{cases} \dot{\boldsymbol{\lambda}}^{E} = \mathbf{0} \\ \ddot{\lambda}_{j}^{E} \geq 0 \\ \ddot{\lambda}_{i\neq j}^{E} = 0 \end{cases} \qquad (23)$$

3. if the internal actions vector is a regular point of the linearized failure surface belonging to the j th hyperplane) and $\dot{\boldsymbol{\lambda}}^{E}(t_0) \neq \mathbf{0}$, we have:

   $$\begin{cases} \dot{\lambda}_{j}^{E} > 0 \\ \dot{\lambda}_{i\neq j}^{E} = 0 \\ \ddot{\lambda}_{j}^{E} \quad \text{free} \\ \ddot{\lambda}_{i\neq j}^{E} = 0 \end{cases} \qquad (24)$$

4. if the internal actions vector is a singular point of the linearized failure surface common to m hyperplanes we have:

   $$\forall \alpha \in [1 \ \ldots \ m] \begin{cases} \ddot{\lambda}_{\alpha}^{E} \geq 0 \quad \textit{if} \quad \dot{\lambda}_{\alpha}^{E} = 0 \\ \ddot{\lambda}_{\alpha}^{E} \quad \text{free} \ \textit{if} \quad \dot{\lambda}_{\alpha}^{E} > 0 \end{cases} \qquad (25)$$

In cases 2 and 3 the internal action vector is represented by any point of the j th hyperplane, whereas for case 4 the internal action state is uniquely determined.

The assembly of all elements transfers the qualitative behavior of a single element (or an interface) to the overall discretized structure. Hence, even the assembled bending moments vector $\tilde{\mathbf{M}}$ remains constant during finite time intervals. In particular, if the vector of external loads is assumed constant during finite time intervals, it can be shown (see for instance Cannarozzi and Laudiero 1976) that the most general motion of a rigid plastic structure results in a sequence of uniformly accelerated motions of finite time interval. The interchange of two consecutive mechanisms is characterized by

a discontinuity of the acceleration fields. Therefore, if we assume to know the set of active yield planes of each element at a given time t_0, for a time step of duration Δt we have:

$$\begin{aligned} \dot{\boldsymbol{\lambda}}_y &> \mathbf{0} \\ \dot{\boldsymbol{\lambda}}_r &= \mathbf{0} \end{aligned} \qquad (26)$$

where index y (r) indicates the vector collecting all the non-zero (zero) plastic multipliers rates in the structure, hence indicating that a yielding condition for a certain element has (has not) been reached. From the previous considerations, differentiation of equation (26) yields:

$$\begin{aligned} \ddot{\boldsymbol{\lambda}}_y &\text{free} \\ \ddot{\boldsymbol{\lambda}}_r &\geq \mathbf{0} \end{aligned} \qquad (27)$$

Hence, leading to the following assembled equation representing first derivative associated flow rule condition:

$$\tilde{\ddot{\boldsymbol{\varepsilon}}}_{pl} - \left[\tilde{\mathbf{A}}^{eqT} \quad \tilde{\mathbf{A}}^{inT}\right] \begin{bmatrix} \ddot{\boldsymbol{\lambda}}_y \\ \ddot{\boldsymbol{\lambda}}_r \end{bmatrix} = 0 \qquad (28)$$

where the aforementioned partition of matrix $\tilde{\mathbf{A}}$ has been already introduced. Exploiting equation (17), a relation between accelerations and second derivatives of plastic multipliers is obtained in the form:

$$\tilde{\mathbf{B}}\ddot{\mathbf{w}} - \left[\tilde{\mathbf{A}}^{eqT} \quad \tilde{\mathbf{A}}^{inT}\right] \begin{bmatrix} \ddot{\boldsymbol{\lambda}}_y \\ \ddot{\boldsymbol{\lambda}}_r \end{bmatrix} = 0 \qquad (29)$$

with corresponding static conditions:

$$\begin{cases} \tilde{\mathbf{A}}^{eq}\tilde{\mathbf{M}} = \tilde{\mathbf{b}}^{eq} \\ \tilde{\mathbf{A}}^{in}\tilde{\mathbf{M}} \leq \tilde{\mathbf{b}}^{in} \\ \tilde{\ddot{\boldsymbol{\lambda}}}_r \left(\tilde{\mathbf{A}}^{in}\tilde{\mathbf{M}} - \tilde{\mathbf{b}}^{in}\right) = 0 \end{cases} \qquad (30)$$

Previous conditions (19)-(28), from well known connections between linear complementarity problems and quadratic programming lead to the formulation reported in (15).The algorithm used to numerically solve the quadratic programming problem (15)-(18) is a modification of the revised simplex method, applied to the LCP problem obtained from (15), by means of the application of Kuhn-Tucker conditions. Details of the algorithm can be found in Jensen and Bard (2003).

5 Numerical simulations: enclosure masonry walls

An enclosure running bond masonry wall of dimensions 5.60×2.80 m (length × height) and subjected to a distributed blast pressure is considered. Bricks are assumed of dimensions 300×200

mm (length × height). The wall is supposed simply supported at the base and on vertical edges, whereas the top edge is assumed unconstrained, due to the typical imperfect connection between infill wall and RC beam. The situation illustrated is typical of enclosure masonry walls in existing buildings in Portugal. Several different thicknesses for the wall are considered, in order to investigate the capabilities of the structure to withstand increasing blast pressures.

In this framework, for the numerical simulations, a number of non linear time-pressure distributions are assumed, as illustrated in Figure 13 (only seven different pressures are depicted for the sake of clearness), corresponding to increasing masses of TNT. Pressure is evaluated with reference to standardized formulas reported in Bangash and Bangash (2006).

In what follows, we assume the mechanical properties summarized in Table I. As it is possible to notice from the table, five different tensile strength values for the joints (labeled from I to V) are investigated, with the aim to analyze the influence of joints limited tensile strength on the overall resistance of the wall when loaded out-of-plane.

For the numerical simulations presented, a linear approximation with 80 planes of masonry strength domain is assumed in the three dimensional sub-space M_{11} - M_{12} - M_{22}. It is assumed, for the sake of simplicity, that membrane actions are equal to zero, except for N_{22}, which is kept equal to one-half of the self weight of the panel (i.e. we assume the typical vertical compression which occurs with good approximation in practice at the mid-height of the wall).

When dealing with a thickness of the wall equal to 150 mm and a tensile strength for the joints equal to 0.10 MPa, a full 3D FE heterogeneous elastic-plastic dynamic analysis has been also conducted, in order to have a deep insight into the problem and to collect alternative data to compare the results with those provided by the present rigid-plastic approach. This latter analysis is what can be possibly performed by practitioners utilizing commercial software. Obviously, it cannot be considered either a reference solution or a standard procedure, due to the approximations introduced in the model and the prohibitive computational effort required. The two different meshes utilized in the homogenized rigid-plastic and the 3D case are depicted in Figure 15-a and –b respectively.

For the heterogeneous 3D model, the commercial software Strand 7.2 (2004) was used to perform the dynamic non-linear analyses. As shown in Figure 15, a relatively refined discretization was adopted, in order to avoid possible inaccuracies due to mesh dependence. A rigid infinitely resistant behavior for bricks was assumed, whereas for joints a Mohr-Coulomb failure criterion with the same tensile strength and friction angle used in the homogenised approach for joints was adopted. Eight-noded brick elements were utilized both for joints and bricks, with a double row of elements along wall thickness.

A comparison between the deformed shapes at t=400 msec obtained with the present model and the commercial software is schematically depicted in Figure 16. As it is possible to notice, the models give almost the same response in terms of deformed shape for the particular instant time inspected (400 msec), confirming that reliable results may be obtained with the model proposed. On the other hand, it is worth underlining that the homogenized rigid plastic model required only 101 seconds to be performed on a standard PC Intel Celeron 1.40 GHz equipped with 1Gb RAM, a processing time around 10^{-3} less expensive with respect to the 3D case. Comparisons on time-maximum displacement curves provided by the two models analyzed is finally reported in Figure 17-a, whereas in Figure 17-b the evolution of the deformation provided by the homogenized model proposed is depicted.

Due to the low computational effort required, full sensitivity analyses are possible even for complex structures, varying both external pressure and constituent materials mechanical properties. In order to put at disposal to practitioners a full set of parametric numerical results for design and safety assessment, a number of analyses are repeated with the model proposed, changing in a wide range (a) mass of explosive (and hence blast pressure profile), (b) masonry mechanical properties (in particular tensile strength) and (c) wall thickness. Figure 18 to Figure 21 illustrate the response of the homogenized rigid-plastic model when subjected to the blast pressures in terms of maximum displacement achieved at the end of the simulations, with a wall thickness ranging from 110 mm (Figure 18) to 300 mm (Figure 21).

For each figure, the results of the sensitivity analysis are obtained ranging the tensile strength from 0.1 to 0.3 MPa (Table I) and the TNT mass from 5 to 70 Kg. As expected, the maximum displacement decreases sensibly when high strength mortar is adopted. Furthermore, it is clear that a mass of 40-50 Kg of TNT produces a final displacement that causes total collapse of the enclosure wall (second order effect are neglected in the present study). On the contrary, displacements ranging from small to medium are achieved in the range 5-25 kg of TNT, meaning that practitioners should decide on the safety assessment of the structure, once that a final admissible displacement is fixed by norms for a given blast pressure. For instance, the Italian norm [33] 3431 (2005) suggests not to exceed a limit displacement equal to 0.3% of the height of the wall (i.e. 8.4 mm in the example here analyzed) in case of seismic action, whereas no specific norm exists dealing with blast loads. In any case, a simple comparison between limit analysis final displacement and maximum displacement allowed (at fixed mass of TNT, wall thickness and masonry strength) is sufficient to establish if the wall is in the safe or unsafe region.

6 Conclusions

A homogenized rigid-plastic plate model for the analysis of masonry plates subjected to blast pressure was presented. Out-of-plane anisotropic masonry failure surfaces have been obtained by means of a compatible kinematic limit analysis approach. In the model, each brick, assumed infinitely resistant, is supposed to interact with its six neighbors by means of mortar joints reduced to interfaces with frictional behavior and with limited tensile and compressive strength. Triangular Kirchhoff-Love elements with linear interpolation of the displacements field and constant moment within each element have been used at a structural level, leading to a discretized quadratic programming formulation at each time step for the analysis of entire walls subjected to blast.

The multi-scale strategy presented has been adopted to predict the behavior of a rectangular wall supported on three sides (left, bottom and right) representing an envelope wall in a building and subjected to a standardized blast load. Comparisons with a standard elastic-plastic approach conducted by means of a commercial FE code were also provided to validate the procedure.

An exhaustive parametric analysis has been finally conducted at different wall thicknesses, joints tensile strength and supposing the plate subjected to increasing dynamic pressures, corresponding to blast loads (in kg of TNT) ranging from small to large.

7 References

[1] Bangash, M.Y.H. and Bangash, T., (2006) *Explosion-Resistant Buildings. Design, analysis and case studies*, Springer.

[2] Begg, D., and Fishwick, R., (1995) Numerical analysis of rigid block structures including sliding, In: Middleton J, Pande G (Eds.), *Computer Methods in Structural Masonry*, 3, pp. 177–183.

[3] Bodner, R.S., and Symonds, P.S. (1962) Experimental and theoretical investigation of the plastic deformation of cantilever beams subjected to impulsive loading. *Journal of Applied Mechanic*s 719.

[4] Burnett, S., Gilbert, M., Molyneaux, T., Beattie, G., and Hobbs, B. (2007) The performance of unreinforced masonry walls subjected to low-velocity impacts: Finite element analysis. *International Journal of Impact Engineering*, 34, pp. 1433-1450.

[5] Cannarozzi, A.A., Laudiero, F. (1976) On plastic dynamic flexure of plates, *Meccanica*, December, pp. 208-218.

[6] Capurso, M. (1972a) A quadratic programming approach to the impulsive loading analysis of rigid plastic structures, *Meccanica*, March, pp. 45-57.

[7] Capurso, M. (1972b) Minimum principles in the dynamics of isotropic rigid-plastic and rigid-viscoplastic continuous media, *Meccanica*, 7(2), pp. 92-97.

[8] Cecchi, A., and Milani, G. (2008) A kinematic FE limit analysis model for thick English bond masonry walls, *International Journal of Solids and Structures*, 45, pp. 1302-1331.

[9] EN 1991-1-7:2006 (2006). *Eurocode 1 - Actions on structures - Part 1-7: General actions - Accidental actions*.

[10] Ferris, M., and Tin-Loi, F. (2001) Limit analysis of frictional block assemblies as a mathematical program with complementarity constraints. *Int. J. Mech. Sci.*, 43, pp. 209-224

[11] Gilbert, M., Hobbs, B., Molyneaux, T.C.K., Melbourne, C., and Watson, A.J. (1998), Laboratory impact testing of free standing masonry walls. *Masonry International*, 11(3), pp. 71-79.

[12] Gilbert, M., Hobbs, B., and Molyneaux, T.C.K. (2002) The performance of unreinforced masonry walls subjected to low-velocity impacts: experiments, *International Journal of Impact Engineering*, 27, pp. 231-251.

[13] Hellan, K. (1967) Analysis of elastic plates in flexure by a simplified finite element method, *Acta Polytech. Scand.*, Ci 46, pp. 1-28.

[14] Herrmann, L.R. (1967) Finite element bending analysis for plates, *J. Eng. Mech. Div. ASCE*, 93, pp.13-26.

[15] Heyman, J. (1969) The safety of masonry arches, *International Journal of Mechanical Sciences*, 43, pp. 209-224.

[16] Jensen, P.A., and Bard, J.F. (2003) *Operations Research Models and Methods*, John Wiley and Sons.

[17] Kim, K.P., and Huh, H. (2006) Dynamic limit analysis formulation for impact simulation of structural members, *International Journal of Solids and Structures*, 43(21), pp. 6488-6501.

[18] Komarov, K.L., and Nemirovskii, Y.V. (1985) Dynamic behavior of rigid-plastic rectangular plates, *International Applied Mechanics*, 21(7), pp. 69-76.

[19] Krabbenhoft, K., and Damkilde, L. (2002) Lower Bound limit analysis of slabs with nonlinear yield criteria, *Computers and Structures*, 80, pp. 2043-2057.

[20] Krabbenhoft, K., Lyamin, A.V., Hjiaj, M., and Sloan, S.W. (2005) A new discontinuous upper bound limit analysis formulation, *International Journal for Numerical Methods in Engineering*, 63, pp. 1069-1088.

[21] Krenk, S., Damkilde, L., and Hoyer, O. (1994) Limit analysis and optimal design of plates with equilibrium elements, *J. Eng. Mech. ASCE*, 120(6), pp. 1237-1254.

[22] Lourenço, P.B., and Rots, J. (1997) A multi-surface interface model for the analysis of masonry structures, *Journal of Engineering Mechanics ASCE*, 123(7), pp. 660-668.

[23] Lourenço, P.B., Rots, J.G., and Blaauwendraad, J. (1998) Continuum model for masonry: parameter estimation and validation, *Journal of Structural Engineering*, 124 (6), pp. 642-652.

[24] Lourenço, P.B. (1999) Anisotropic softening model for masonry plates and shells, *Journal of Structural Engineering ASCE*, 126(9), pp. 1008-1016.

[25] Martin, J.B. (1964) Impulsive loading theorems for rigid-plastic continua, *Proc. Eng. Mech. Div. ASCE*, E.M. 5 90, pp. 27.

[26] Martin, J.B., and Ponter, A.S. (1972) Bounds on large deformations of impulsively loaded elastic-plastic structures. *Proc. ASCE*, E.M. 1, pp. 107.

[27] Martin, J.B., and Symonds, P.S. (1965) Mode approximations for impulsively loaded rigid-plastic structures, *Brown University Report, Division on Engineering, Providence*, pp. 1-61.

[28] Mayrhofer, C. (2002) Reinforced masonry walls under blast loading, *International Journal of Mechanical Sciences*, 44, pp. 1067-1080.

[29] Milani, G., Lourenço, P.B., and Tralli, A. (2006a) Homogenised limit analysis of masonry walls. Part I: failure surfaces, *Computers and Structures*, 84, pp. 166-180.

[30] Milani, G., Lourenço, P.B., and Tralli, A. (2006b) Homogenised limit analysis of masonry walls. Part II: structural examples, *Computers and Structures*, 84, pp. 181-195.

[31] Milani, G., Lourenço, P.B., and Tralli, A. (2006c) Homogenization approach for the limit analysis of out-of-plane loaded masonry walls, *Journal of Structural Engineering ASCE*, 132 (10), pp. 1650-1663.

[32] Munro, J., Da Fonseca, A.M.A. (1978) Yield-line method by finite elements and linear programming, *J. Struct. Eng. ASCE*, 56B, pp. 37-44.

[33] O.P.C.M. 3431/05 09/05/2005 (2005). Further modifications and integrations on OPCM 3274/03" [in Italian], Ulteriori modifiche ed integrazioni all'OPCM 3274/03.

[34] Orduña, A., and Lourenço, P.B. (2005) Three-dimensional limit analysis of rigid blocks assemblages. Part I: Torsion failure on frictional joints and limit analysis formulation, *Int. J. Solids and Structures*, 42 (18-19), pp. 5140-5160

[35] Sinha, B.P. (1978) A simplified ultimate load analysis of laterally loaded model orthotropic brickwork panels of low tensile strength, *Journal of Structural Engineering ASCE*, 56B(4), pp. 81-84

[36] Strand 7.2 (2004) *Theoretical Manual*. www.strand7.com Sydney Australia, pp. 1-410.

[37] Suquet, P. (1983) Analyse limite et et homogeneisation, *Comptes Rendus de l'Academie des Sciences - Series IIB – Mechanics*, 296, pp. 1355-1358.

[38] Tamuzh, V.P. (1962) On a minimum principle in dynamics of rigid-plastic bodies, *Prikl. Math. Mek.*, 26, pp. 1067.

[39] Wu, C., Hao, H. (2006) Derivation of 3D masonry properties using numerical homogenization technique, *International Journal for Numerical Methods in Engineering*, 66, pp. 1717-1737.

[40] Wu, C., Hao, H. (2008) Numerical derivation of averaged material properties of hollow concrete block masonry, *Engineering Structures*, 30, pp. 870-883.

8 Figures

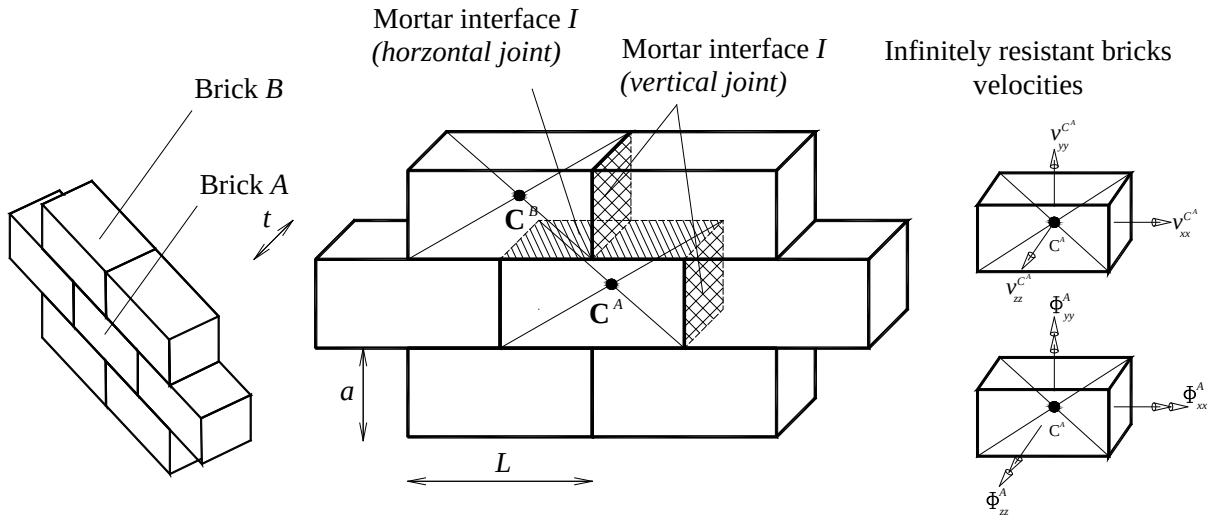

Figure 1: Masonry kinematic model. Two adjacent bricks (A, centroid $\mathbf{C}^A$ and B, centroid $\mathbf{C}^B$) connected by means of a mortar interface I where plastic dissipation occurs. For each brick three velocities unknowns and three rotation rates must be introduced in the optimization problem at a cell level (infinite strength of bricks hypothesis).

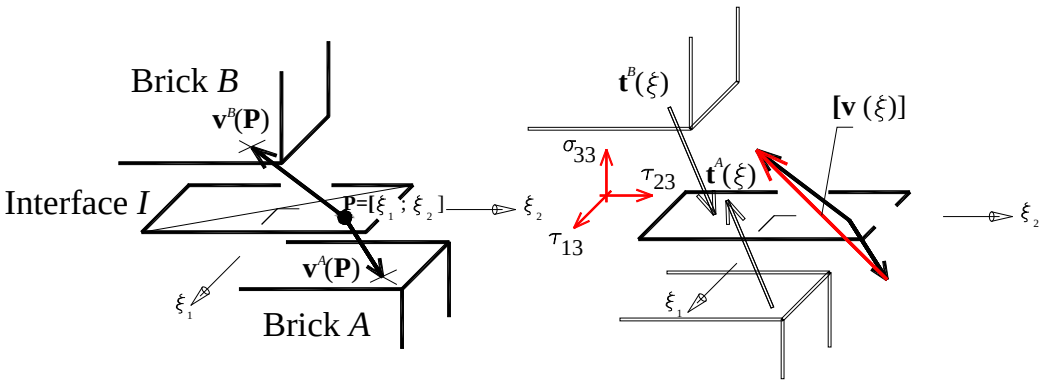

Figure 2: Jump of velocities and stress field acting on an interface I between contiguous bricks A and B.

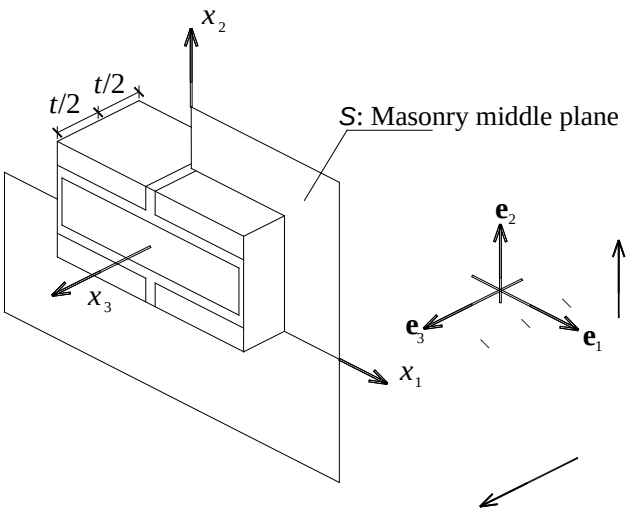

Figure 3: Reference surface chosen for masonry.

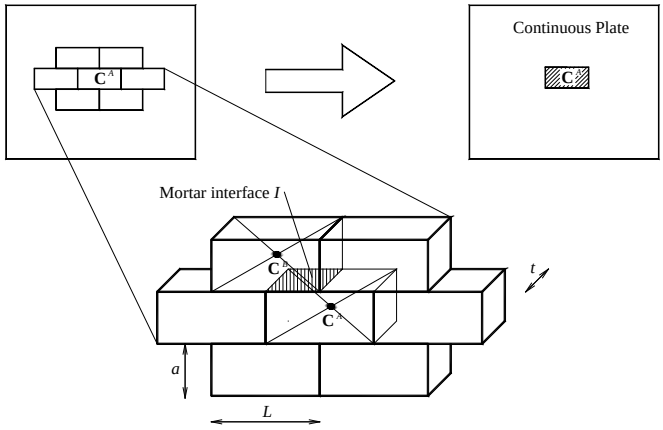

Figure 4: Representative volume element and identification between discrete model and continuous model.

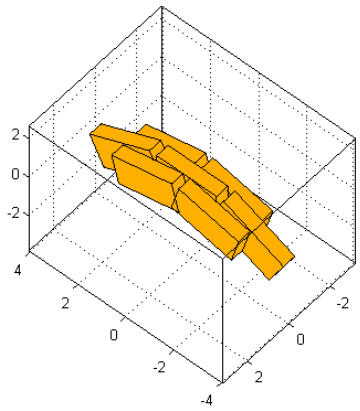

-a

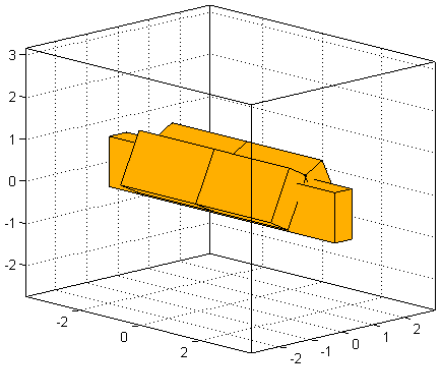

-b

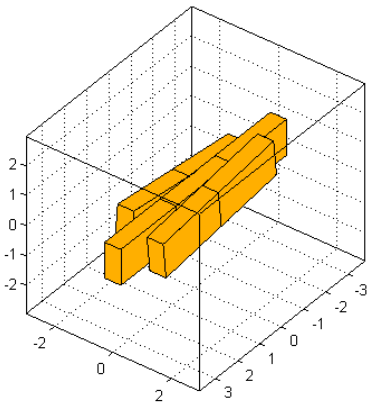

-c

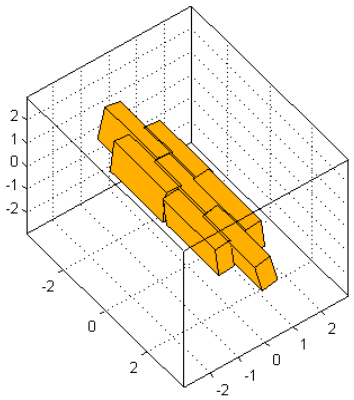

-d

Figure 5: Elementary homogeneous deformations applied to the representative volume element. –a: $\dot{\chi}_{11}$. –b: $\dot{\chi}_{22}$. –c: $\dot{\chi}_{12}$. –d: $\dot{\chi}_{21}$.

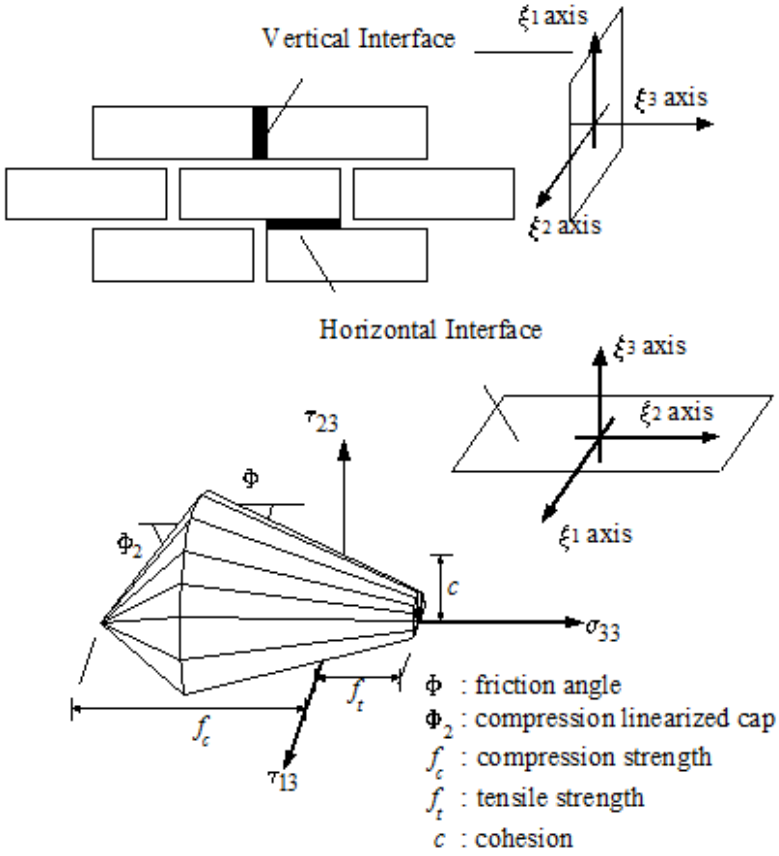

Figure 6: Piecewise linear approximation of the failure criterion adopted for joints. Mohr-Coulomb failure criterion with tension cut-off and linearized compression cap.

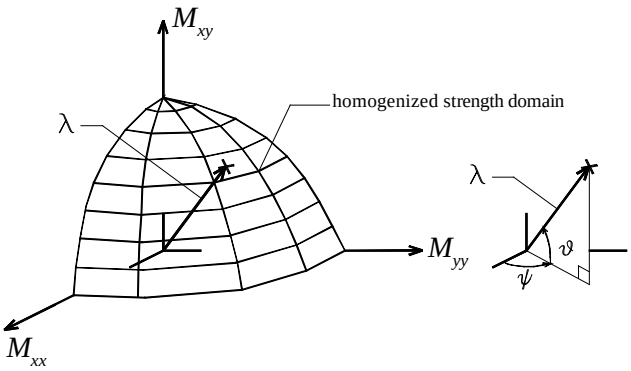

Figure 7: Meaning of λ multiplier in the optimization problem and ψ and ϑ angles.

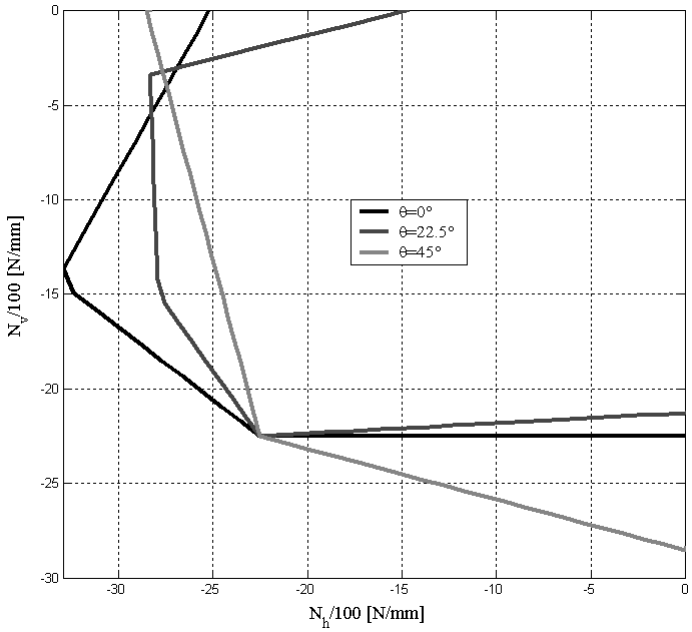

-a

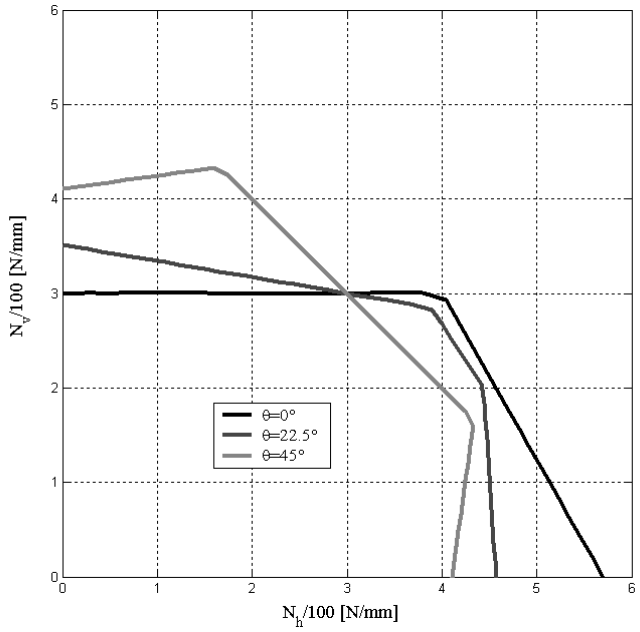

-b

Figure 8: Homogenized masonry failure surfaces (in-plane sections at different orientations of the load with respect to the bed joint).

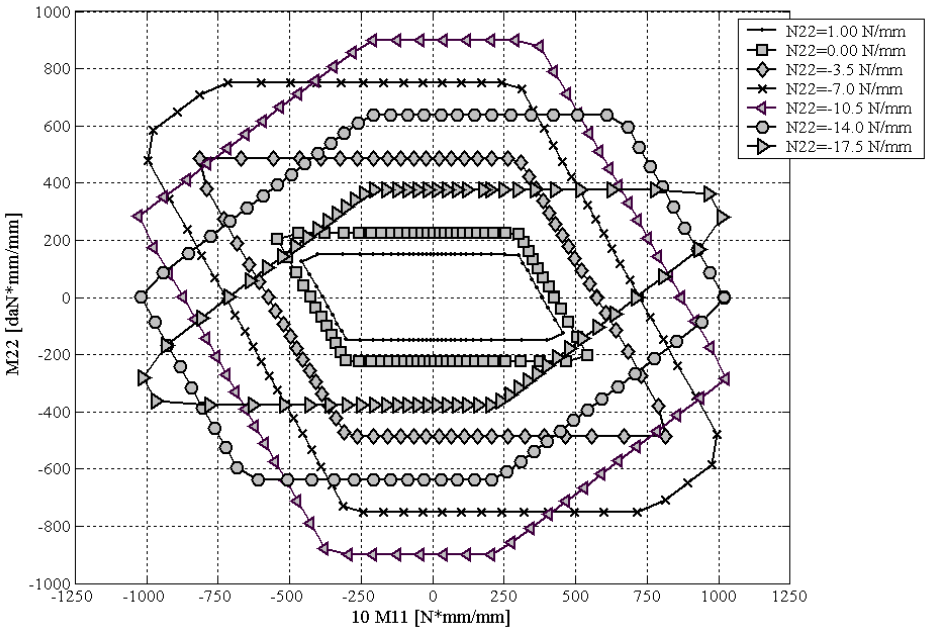

-a

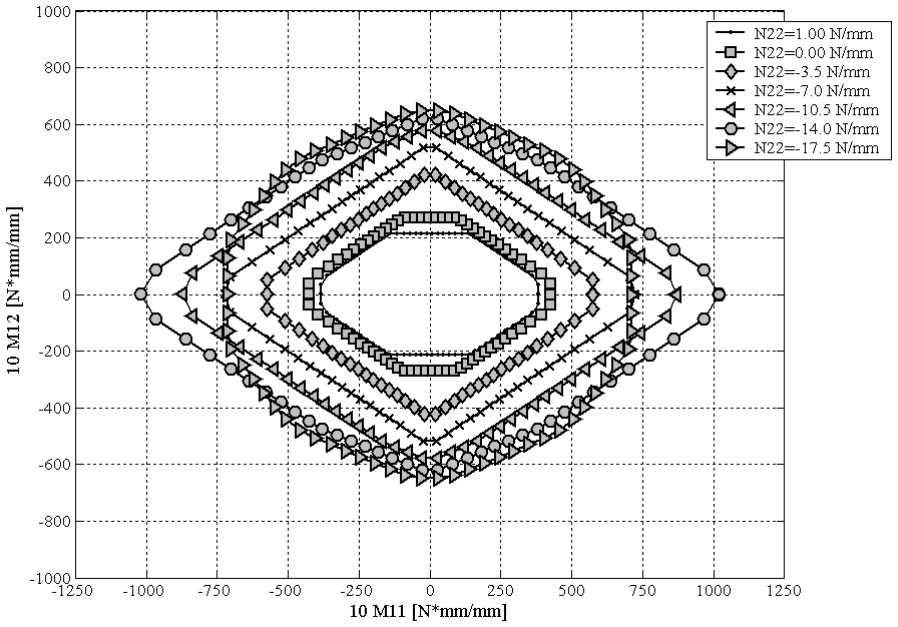

-b

Figure 9: Out-of-plane homogenized failure surfaces at increasing axial vertical compressive loads. –a: M11-M22. –b: M11-M12.

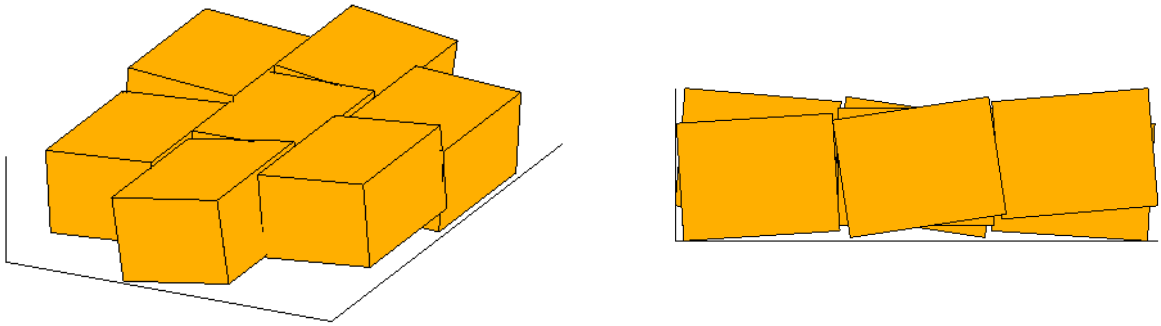

Figure 10: Typical deformed shape at collapse obtained with the kinematic model proposed in case of pure torsion.

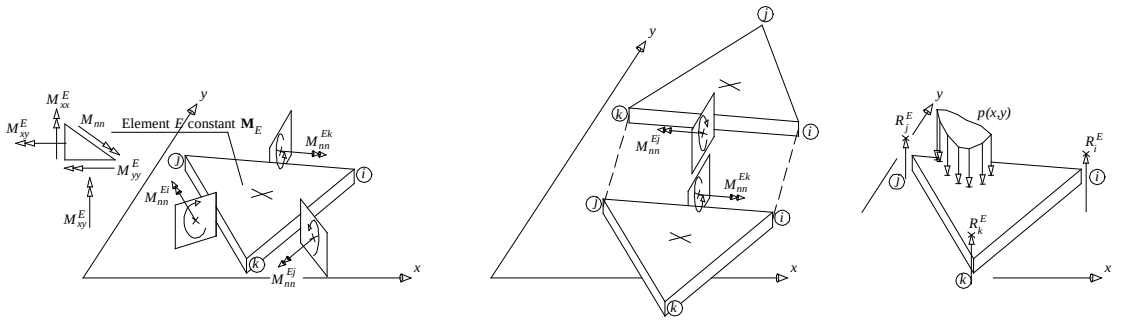

-a -b -c

Figure 11: Bending moment acting at the edges of the triangular plate element used for the FE rigid-plastic analysis (-a), continuity of the bending moment on interfaces (-b), integral equilibrium (-c).

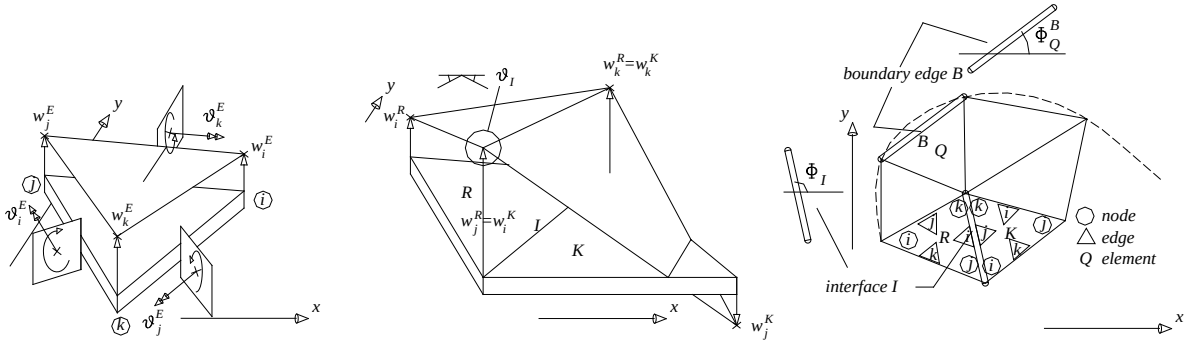

-a -b -c

Figure 12: Rotations at the edges of the triangular plate element used for the FE rigid-plastic analysis (-a), mutual rotation along an interface between adjacent triangles (-b), discretization of the 2D domain (-c).

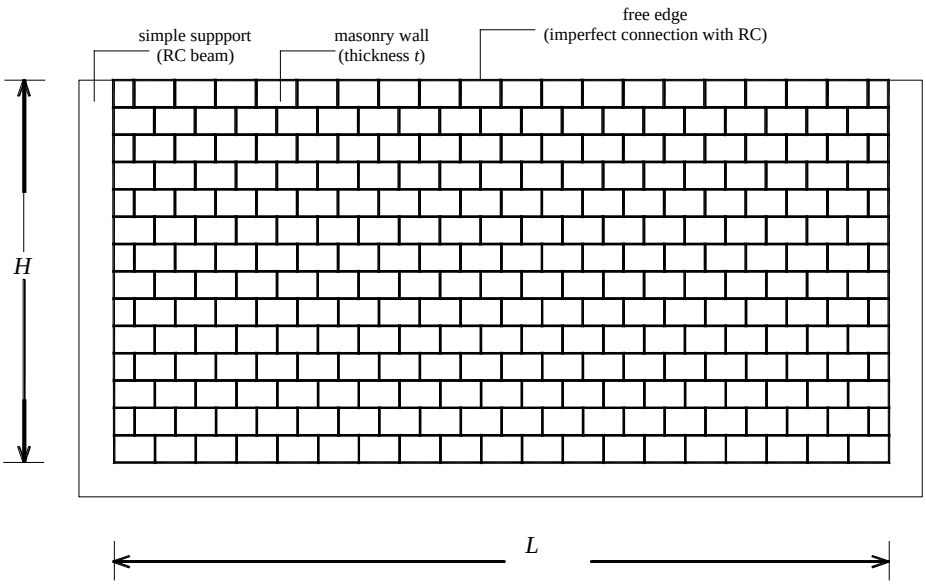

Figure 13: Stretcher bond masonry infill wall. Geometry and boundary constraints

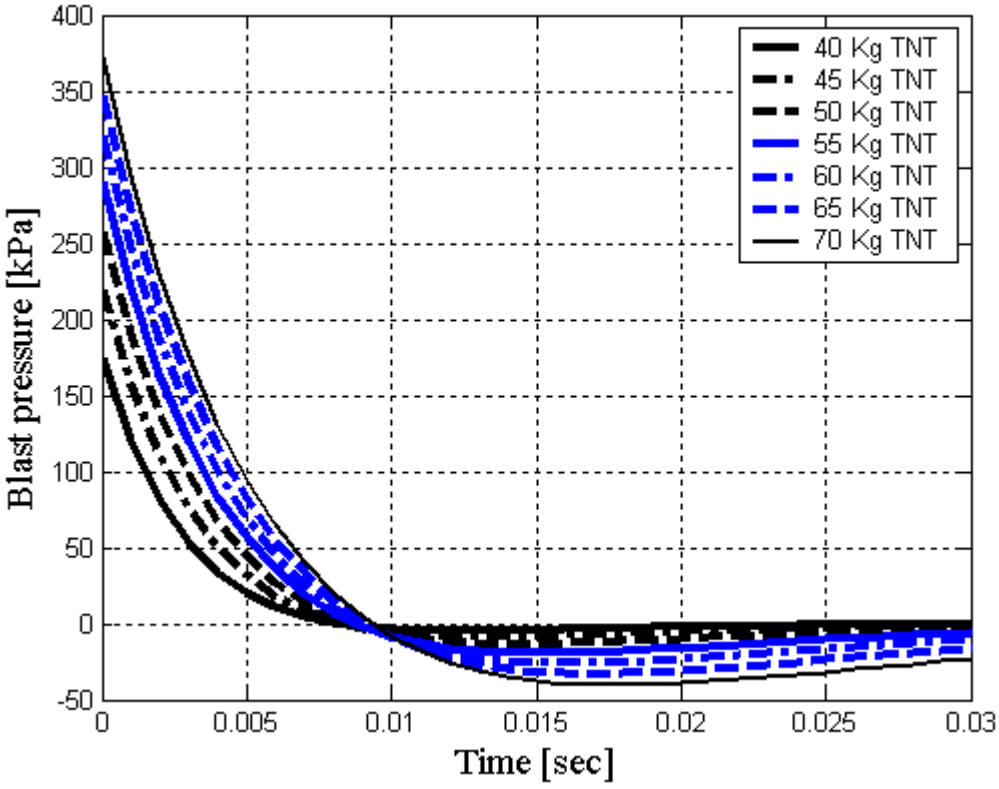

Figure 14: Blast pressures applied to the FE rigid-plastic model.

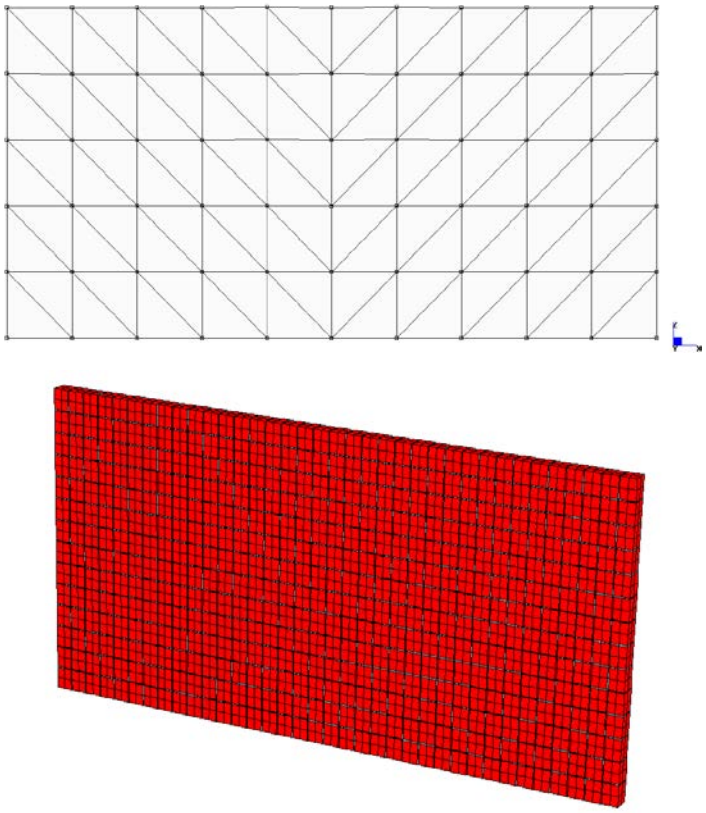

-a

-b

Figure 15: Stretcher bond masonry parapet subject to low velocity impact.–a: FE limit analysis discretization. –b: elastic-plastic heterogeneous 3D model.

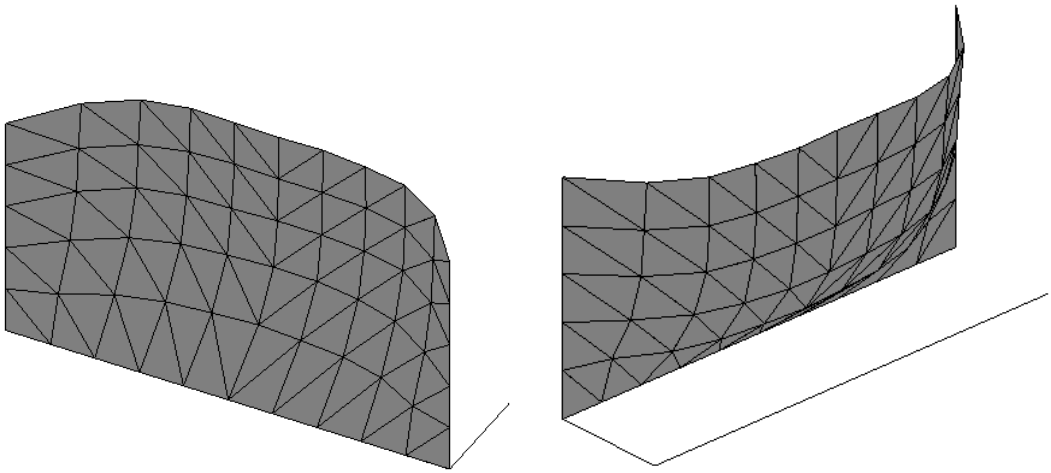

-a

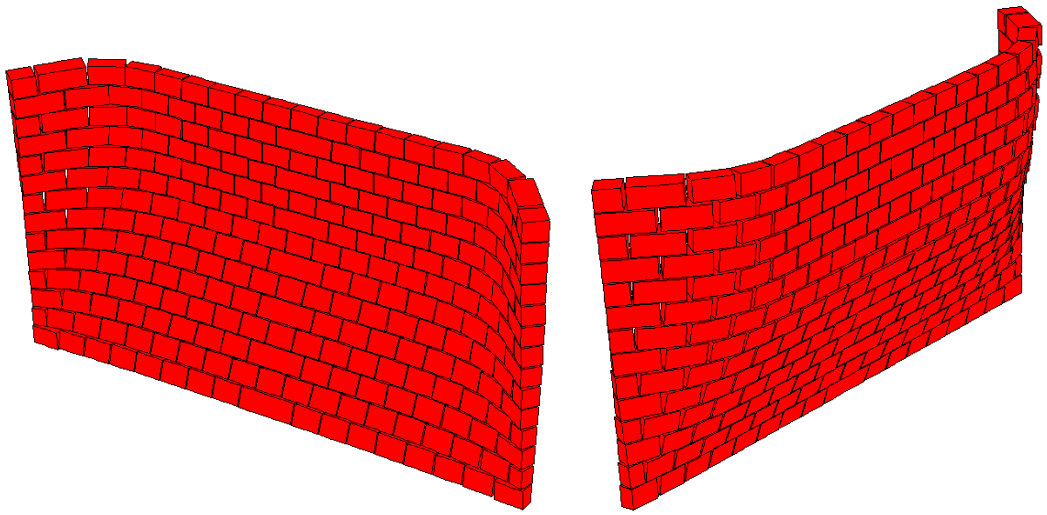

-b

Figure 16: Stretcher bond masonry infill wall subjected to blast pressure. Comparison among deformed shapes at t=400 msec –a: Homogenized limit analysis approach. –b: heterogeneous 3D elastic-plastic FE approach. Mortar joint tensile strength f_t =0.1 MPa, 50 Kg TNT, thickness 150 mm.

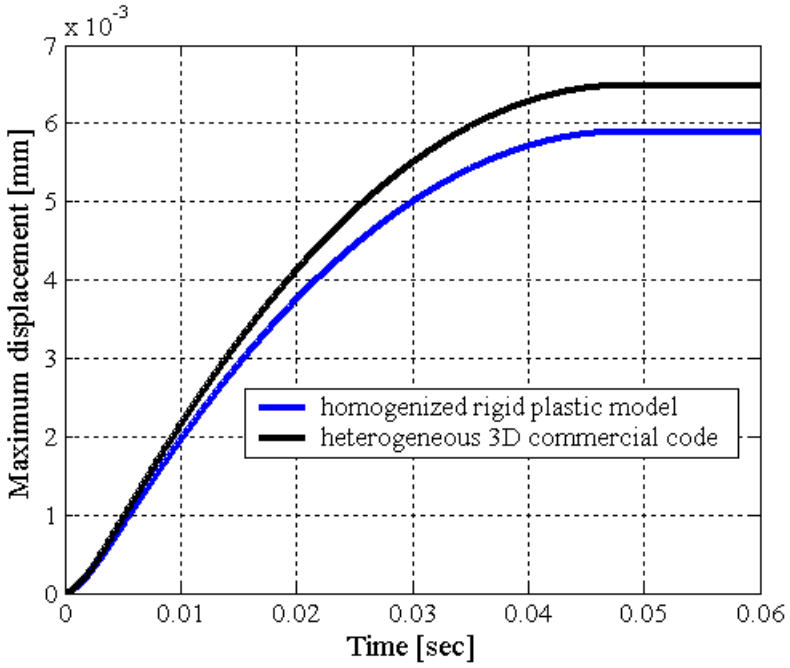

-a

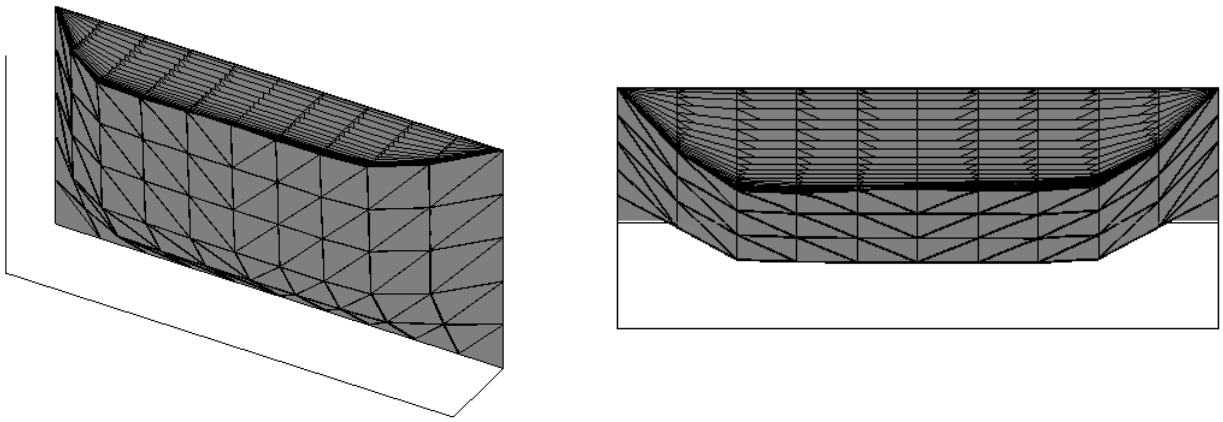

-b

Figure 17: Infill masonry wall subjected to blast. Results from the rigid-plastic model. –a: maximum displacement-time diagram with a comparison with the 3D commercial software. –b: perspective and aerial view of deformed shape evolution. Mortar joint tensile strength f_t =0.1 MPa, 25 Kg TNT, thickness 150 mm.

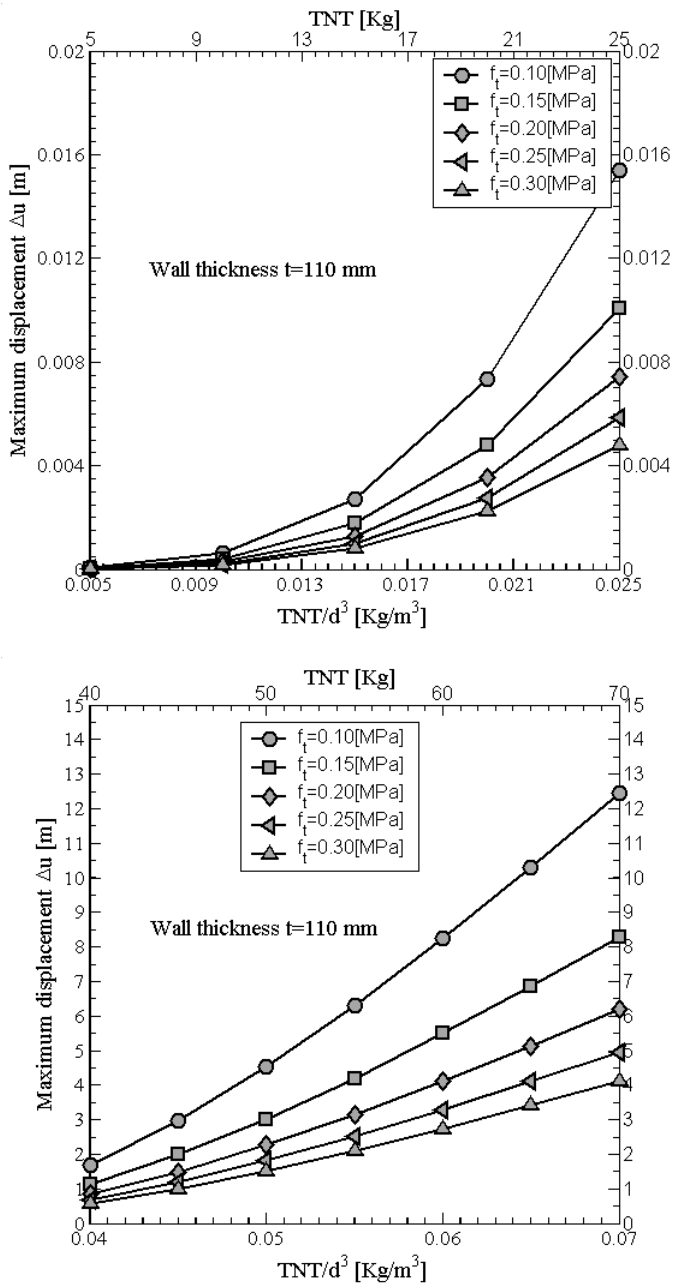

Figure 18: Thickness 110 mm. TNT blast load vs maximum displacement at different values of mortar tensile strength.

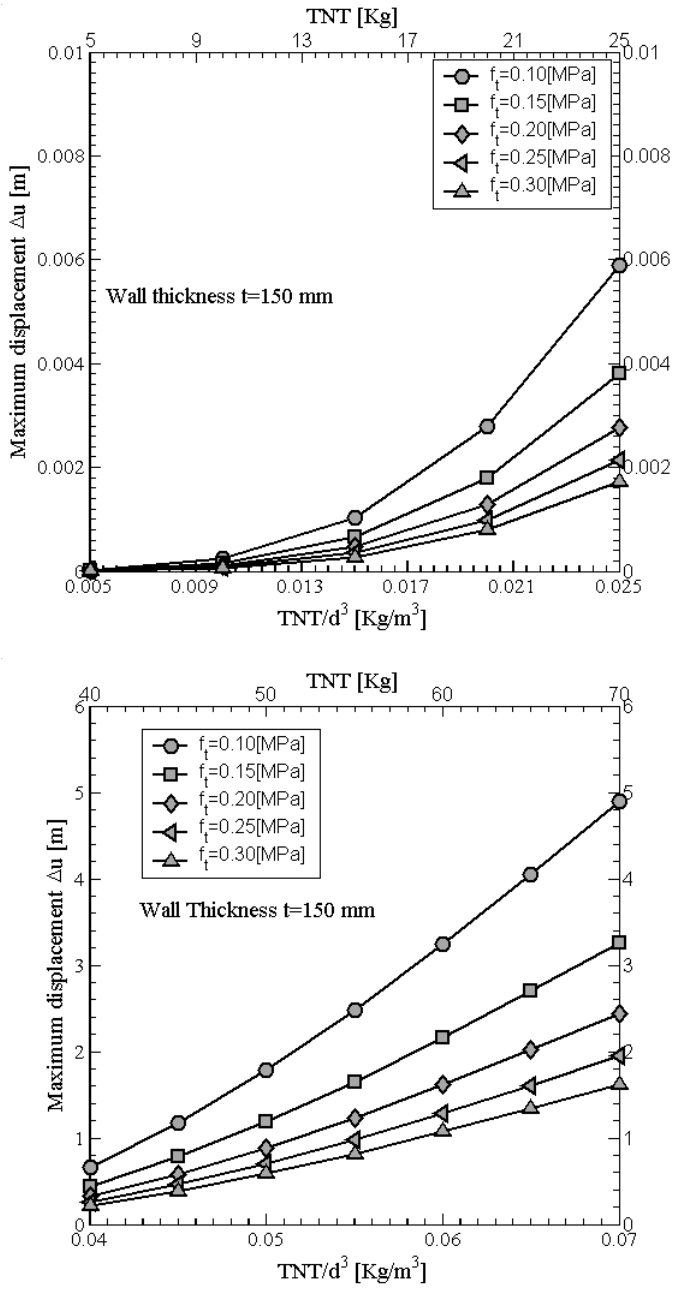

Figure 19: Thickness 150 mm. TNT blast load vs maximum displacement at different values of mortar tensile strength.

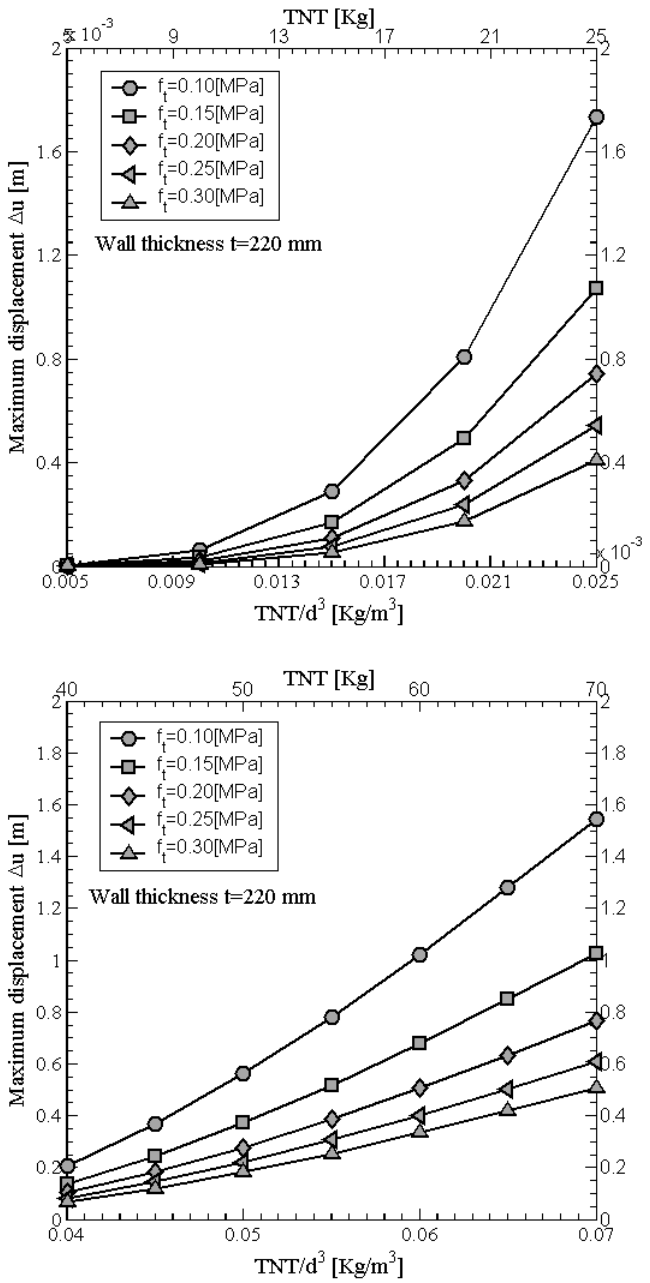

Figure 20: Thickness 220 mm. TNT blast load vs maximum displacement at different values of mortar tensile strength.

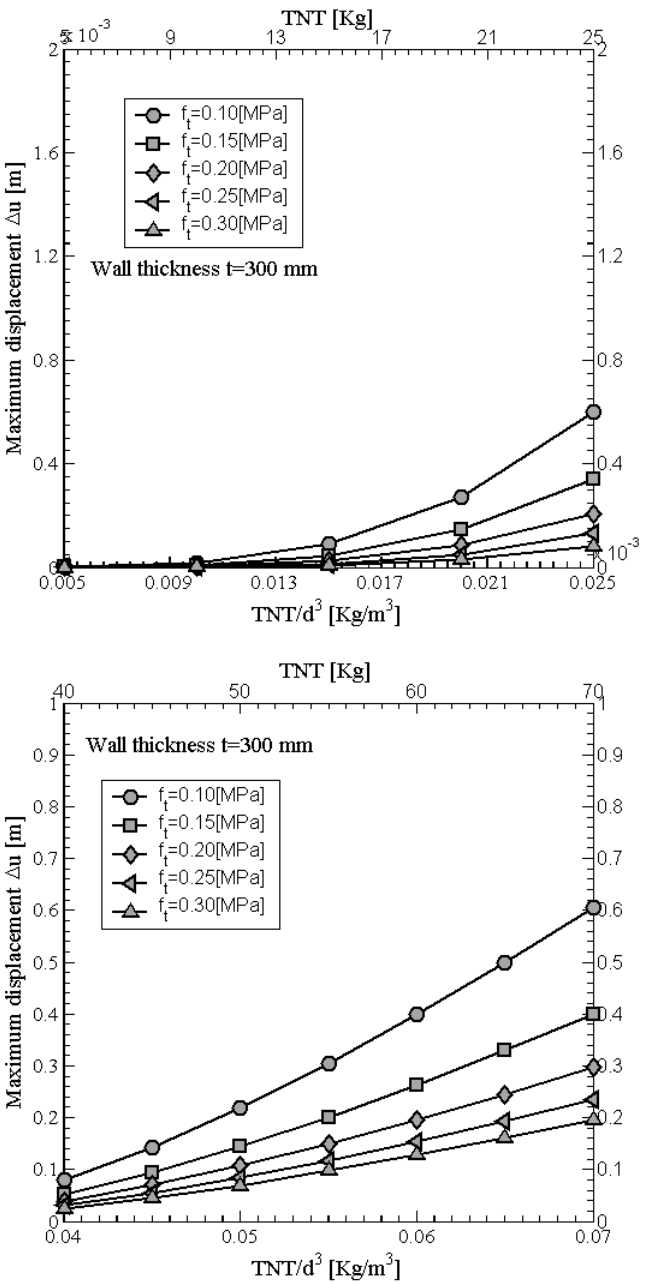

Figure 21: Thickness 300 mm. TNT blast load vs maximum displacement at different values of mortar tensile strength.

9 Tables

Table I: Mechanical characteristics assumed for bricks-mortar joints (f_t: tension cut-off, c : cohesion, Φ: friction angle, f_c: compressive strength, Φ_2: shape of the linearized compressive cap).

f_t MPa					c	Φ	f_c MPa	Φ_2
I	II	III	IV	V				
0.10	0.15	0.20	0.25	0.30	1.2 f_t	37°	15	60°